Revision 1

Title: Chemistry-dependent Raman spectral features of glauconite and nontronite: Implications for mineral identification and provenance analysis

Short title: Raman spectral features of glauconite and nontronite

Raphael J. Baumgartner[1,2*], Javier Cuadros[3], Joseph Michalski[4], Bobby Pejcic[1], Carsten Laukamp[1], Siyu Hu [1], Julien Bourdet[5]

[1]*CSIRO Mineral Resources, Australian Resources Research Centre, Kensington, WA, Australia.*

[2]*School of Biological, Earth and Environmental Sciences, The University of New South Wales, Kensington, NSW, Australia.*

[3]*Department of Earth Sciences, The Natural History Museum, London, United Kingdom.*

[4]*Department of Earth Sciences and Laboratory for Space Research, University of Hong Kong, Hong Kong, China.*

[5]*CSIRO Energy, Australian Resources Research Centre, Kensington, WA, Australia.*

*Corresponding author (raphael.baumgartner@csiro.au; +61 4 235 36 167)

KEYWORDS

Phyllosilicates; Glauconite; Nontronite; Peak shift

ABSTRACT

This study provides a comprehensive Raman spectral characterization of nontronite and glauconite-nontronite mixed-layer phases from seafloor hydrothermal fields. These 2:1 phyllosilicates, which show isomorphous cation exchange between Mg^{2+}+Fe^{2+} and Fe^{3+}+Al^{3+} in the dioctahedral sheets, exhibit three diagnostic Raman peaks in the low-wavenumber

region (v1 ~241-257 cm^{-1}; v2 ~600-606 cm^{-1}; v3 ~690 cm^{-1}), and one peak at ~3548-3570 cm^{-1} (v4). With increasing $(Mg^{2+}+Fe^{2+})_{oct}$, the presumed stretching band of octahedral OH-O bonds (v1) is displaced to higher wavenumber, whereas the stretching band of tetrahedral Si-O-Si bonds (v2) is shifted to lower wavenumber. Peak v4, which relates to O-H bonds of hydroxyls linked to octahedral cations, shows a downshift with increasing $(Mg^{2+}+Fe^{2+})_{oct}$. The deconvolution of v4 indicates three maxima, two of which strongly correlate with the cation occupancy in the octahedral sheets; i.e., vibrations of hydroxyls linked to trivalent cations (Fe^{3+} and Al^{3+}) are mainly represented by a band at ~3560-3573 cm^{-1}, whereas divalent cations (Mg^{2+} and Fe^{2+}) mainly contribute to a band at ~3538-3540 cm^{-1}. This result is consistent with theoretical considerations for dioctahedral phyllosilicates, which predict for the incorporation of $Mg^{2+}$and Fe^{2+} a weakening/lengthening of O-H bonds in the OH groups, accounting for a downshift of the O-H vibrations. Hence, this is one of the first studies that traces how even subtle chemical modifications in phyllosilicates influence Raman spectral features. The reported findings have implications for mineral identification and provenance analysis, such as during surface exploration on Mars, where compositionally diverse phyllosilicates occur.

INTRODUCTION

Raman spectroscopy found widespread application in the rapid and non-destructive characterization of silicate minerals (Griffiths, 1969; Blaha and Rosasco, 1978; Michaelian, 1986; McMillan, 1989; Tlili, 1989; Kuebler et al., 2006; Bersani et al., 2009; Wang et al., 2001, 2015; Kloprogge, 2017). However, a detailed understanding of the Raman spectral features of many phyllosilicates is still lacking (cf., Wang et al., 2015; Kloprogge, 2017). This holds true for glauconite and nontronite, 2:1 phyllosilicates that belong to the mica and smectite groups, respectively. These minerals show the commonality of having layers of octahedral sheets [trivalent metals (Fe^{3+} and Al^{3+}) and divalent metals ($Mg^{2+} > Fe^{2+}$) bound to

48 O and OH; $MO_4(OH)_2$] sandwiched by two tetrahedral sheets [Si, Fe^{3+}, and Al^{3+}, which are
49 coordinated with oxygen; $(Si,Al^{3+},Fe^{3+})O_4$]. In glauconite, the substition of Al^{3+} for
50 tetrahedral Si^{4+} accounts for a high layer charge that is balanced by interlayer K^+, whereas the
51 lower layer charge in nontronite attracts higher charged metal cations that are fully hydrated
52 (i.e., Na^+, Mg^{2+} and Ca^{2+}).

53 Both nontronite and glauconite are dioctahedral phyllosilicates. In other words, most
54 octahedral cations are trivalent, and hence approximately two out of the three sites in their
55 structural formula [based on a $O_{10}(OH)_2$ anion framework] are occupied (Fig. 1). By
56 comparison, phyllosilicates dominated by divalent cations are termed trioctahedral, because
57 essentially all the three octahedral sites are occupied. This change in cation occupancy
58 accounts for a contrasting configuration of the surrounding OH groups: i) in dioctahedral
59 sheets, the OH vector is tilted at a relatively low angle relative to the plane of octahedral
60 sheets, and directed towards the unoccupied site (Fig. 1); ii) in trioctahedral sheets, the OH
61 vector is oriented perpendicular to the plane of the octahedral sheets. Such differences can
62 influence O-H stretching (ν) and bending (δ) vibrations in the octahedral domains, and even
63 vibrations in the interlinked tetrahedral sheets. The corresponding bands in Raman
64 spectroscopy and infrared (IR) spectroscopy have been extensively studied (Daynyak et al.,
65 1992; Madejová et al., 1994; Frost and Rintoul, 1996a,b; Besson and Drits 1997a,b; Drits et
66 al. 1997; Frost and Kloprogge, 2000a,b; Bishop et al., 2002a, 2002b, 2008; Madejová, 2003;
67 Petit et al., 2004; Zviagina et al., 2004; Cuadros et al., 2013, 2016, 2019; Michalski et al.,
68 2015; Wang et al., 2015; Kloprogge et al., 2017). However, the spectral features are not only
69 sensitive to such major structural changes, they are also influenced by even subtle
70 compositional variations (cation exchange) in both the tetrahedral and octahedral sheets. In
71 Raman spectroscopy, the relating band shifts were studied for a variety of silicate minerals,
72 such as garnet, olivine, or pyroxene (Wang et al., 2001; Kuebler et al., 2006; Bersani et al.,

2009), whereas similar effects in phyllosilicates are largely unexplored (cf., Wang et al., 2015).

Previous Raman spectroscopy studies of nontronite and glauconite established a baseline for discriminating their main spectral features in relation to fundamental structural and chemical properties (Frost and Kloprogge, 2000a,b; Ospitali et al., 2008; Wang et al., 2015; Kloprogge, 2017). However, in contrast to the detailed understanding of their IR characteristics, determining the relations between Raman spectral features and variations in octahedral cation occupancy remained elusive. In fact, this endeavour must rely on the extensive characterization of glauconite and nontronite with a wide range of structural and chemical properties, but such materials are difficult to access. To fill these knowledge gaps, this study reports a comprehensive Raman spectral characterization of nontronite and glauconite-nontronite mixed-layer phases (i.e., vertical mixing/interstratification of glauconite and nontronite layers) from seafloor hydrothermal fields. We show that the analyzed samples exhibit distinctive and systematic differences in Raman spectral features relating to the exchange of divalent and trivalent metal cations (Mg^{2+}+Fe^{2+} for Fe^{3+}+Al^{3+}) in the octahedral sheets. The importance of these findings for a variety of technical applications on Earth, and in the surface exploration of other telluric planets in the solar system, especially Mars, is discussed.

MATERIAL AND METHODS

The nontronite and glauconite-nontronite mixed-layer phases examined in this study are from seafloor hydrothermal fields of the Atlantis II Deep (Red Sea) and East Pacific Rise (Pacific Ocean); see Table 1. Their geologic context, mineralogy, and chemistry (including Fe^{2+}/Fe^{3+} ratios), were reported in detail in Cuadros et al. (2013), in which they were characterized using X-ray diffraction analysis (XRD), inductively coupled plasma atomic emission spectroscopy analysis (ICP-AES), thermal gravimetry-evolved gas analysis (TG-EGA),

Mössbauer Spectroscopy, scanning electron microscopy (SEM), and transmission MIR spectroscopy; see additional IR spectroscopy data of these phyllosilicate materials in Michalski et al. (2015) and Cuadros et al. (2016). Besides the differences in mineralogy and the contrasting proportions of glauconite and nontronite, these materials also show variable substitution of Mg^{2+}+Fe^{2+} for Fe^{3+}+Al^{3+} in the octahedral sheets (Table 1); they are thus termed as high $(Mg^{2+}+Fe^{2+})_{oct}/M_{oct}$ and low $(Mg^{2+}+Fe^{2+})_{oct}/M_{oct}$ samples for the sake of comparison and discussion of the acquired spectroscopic data.

Here, these phyllosilicate samples are analyzed using scanning electron microscopy (SEM), as well as Raman spectroscopy and NIR reflectance spectroscopy. For this purpose, the previously prepared, grounded, and purified samples (cf., Cuadros et al., 2013), were attached to silica glass slides using double-sided adhesive tape, by letting the powdered materials fall onto the tape and carefully fixing them with hand pressure. Nontronite and glauconite-nontronite grains that were deemed suitable for SEM analysis and spectroscopic measurements were then selected using a Zeiss Axio Imager.A2 microscope.

Backscattered electron (BSE) and secondary electron (SE) imagery, as well as element analysis by Energy Dispersive X–ray Spectroscopy (EDS), was performed using a FEI XHR–Verios 460l field–emission SEM installed at the Centre for Microscopy, Characterisation and Analysis (CMCA), University of Western Australia (UWA), and a Tescan Mira3 FEG-SE installed at CSIRO Mineral Resources, Kensington, Western Australia. For this purpose, the phyllosilicate samples mounted to glass slides using adhesive tape were carbon coated (~30 nm thick layer). Both BSE and SE images were then acquired using 10–15 keV acceleration voltage and 0.1–0.2 nA beam current, whereas EDS spot analysis, which was carried out in Oxford Instruments' Aztec software, involved 15 keV accelation voltage, 0.2 nA beam current, and 60-120 s measurement time.

Infrared reflectance spectroscopy measurements of the mineral grains attached to glass slides were performed using a Vertex 70 Fourier transform IR spectrometer (Bruker) and a Hyperion 3000 microscope. The analyses were performed using a 15× objective and a mercury-cadmium-telluride (MCT) detector. The microscope is equipped with a video camera for image display, and a computer-controlled stage for automated mapping. Spectra were recorded from an area of ~30×30 μm. A smaller aperture size was not used because it would result in poor quality spectra with unacceptable signal-to-noise ratios. All spectra were collected using 1200 scans and 2 cm^{-1} spectral resolution in the 600-7500 cm^{-1} range. Background spectra were obtained on a gold plate using the same analytical conditions. All measurements were performed at room temperature (20 ± 2 ºC). The IR absorption features were determined in MagicPlot (MagicPlot Systems LLC, Saint Petersburg, Russia).

Raman spectroscopy analysis was carried out at CSIRO Mineral Resources, using a Horiba LabRam HR Evolution instrument, which is equipped with a multichannel air cooled (-70 ˚C) Synapse Visible detector, and a 100 mW continuous wave single frequency (532 nm) diode laser from Laser Quantum. Spot analyses on selected phyllosilicate grains were acquired at room temperature (20 ± 2 ºC), using a 100× objective, which allows focusing of the unpolarized laser beam to a width of approximately 0.72 μm. Filtering (5-10%) decreased the laser power to ~1 mW on the sample surface. This low laser power was used to avoid Raman signal alteration by sample heating and thermal damage. The spectra were collected with 600 grooves/mm, using 2s exposure time and 100-300 accumulations in the low-wavenumber region (<1800 cm^{-1}), and using 2s exposure time and 500-2000 accumulations in the hydroxyl stretching region (3000-4200 cm^{-1}). These relatively long acquisition times were necessary because phyllosilicates are moderate to weak Raman scatterers, particularly in the case of small particle/crystal sizes, as in the analyzed samples. The Raman bands were calibrated against characteristic peaks of a Si wafer and a neon lamp. Baseline correction was

done in Horiba's LabSpec software using third- or fourth-degree polynomial functions fitted to spectral intervals that contain background but no discernible peaks.

The positions of Raman peaks in the low-wavenumber region (<1000cm^{-1}; v1, v2, and v3; Table 2), and the parameters (positions, areas, heights, and full widths at half maximum) of bands that make up a broad hydroxyl peak at ~3500-3700 cm^{-1} (v4; Table 2), were determined in MagicPlot. The latter peak was decomposed by curve-fitting using Gaussian peak functions. Although Raman bands of minerals are unlikely to have pure Gaussian profiles, this curve type is advantageous in that its flanks decrease sharply to produce well-constrained fitting results. The number of bands used for fitting of v4 was three (hereafter vA, vB and vC), as determined on basis of distinctive peak asymmetries and shoulders/tails.

The fitting calculations involved the following steps. First, the positions of vA, vB, and vC, were approximated by consideration of the overall position and shape of v4 (step 1): i) for low $(Mg^{2+}+Fe^{2+})_{oct}/M_{oct}$ samples, vA = 3542 cm^{-1}, vB = 3572 cm^{-1}, and vC = 3610 cm^{-1}; ii) for high $(Mg^{2+}+Fe^{2+})_{oct}/M_{oct}$ samples, vA = 3539 cm^{-1}, vB = 3560 cm^{-1}, and vC = 3600-3605 cm^{-1}. Second, multiple calculation steps were carried out by keeping selected parameters locked, although occasional hand adjustment was necessary to correct for implausible/unacceptable calculation results. Initially, the area, height, and half width at half maximum (HWHM) of each band was calculated in a single iteration step after locking the estimated positions of all bands (step 2). Because vC is the least well resolved band in most spectra, its parameters were then calculated by keeping all parameters of vA and vB fixed (step 3). Next, calculation was redone by keeping only the areas of the peaks locked (step 4). However, this step did not provide meaningful results for some of the samples with high $(Mg^{2+}+Fe^{2+})_{oct}/M_{oct}$. In these instances, the step 4 was split into two steps. First, the band parameters were calculated by keeping both the area and HWHM of vA and vB fixed. Second, the HWHM of both vA and vB was released, but the newly calculated positions

172 locked. The utilized spectral deconvolution strategy consistently provided r^2 values of >0.999
173 between the original and calculated spectra.

174 **RESULTS**

175 *Mineralogy and chemistry*

176 The mineralogical and chemical characteristics of the analyzed samples are documented in
177 detail in Cuadros et al. (2013). In this study, both SEM imagery and qualitative EDS spot
178 analysis (Fig. 2 and 3) was used to ensure that Raman spectra were acquired on (near-) pure
179 phyllosilicate areas, and to examine micro-mineralogical and chemical variations within the
180 samples.

181 The SEM images reveal that all analyzed samples comprise irregularly shaped
182 nontronite or glauconite-nontronite grains up to several hundreds of micro-meters in diameter
183 (Fig. 2a). These grains essentially consist of stacked or tortuous, lower micron- to nanoscale,
184 platy to fibrous particles that are commonly assembled in partially crackled, sheath- to rope-
185 like order. Besides variations in particle size, all samples exhibit very similar morphological
186 habits; i.e., no distinctive differences were observed between high and low
187 $(Mg^{2+}+Fe^{2+})_{oct}/M_{oct}$ samples (Fig. 2). Owing to careful sample preparation/purification,
188 contaminating mineral particles are scarce or entirely absent; see the accessory Fe-hydroxide
189 and/or Cu-rich phases in Fig. 2b-d. Qualitative EDS point analysis of glauconite-nontronite
190 grains in each sample – see the exemplary data for Va22-146KS-612-614 and 1183-15 in Fig.
191 3 – broadly match the corresponding bulk compositional data reported in Cuadros et al.
192 (2013) and summarized in Table 1. Moreover, a series of EDS analyses on multiple grains
193 within each sample illustrate their (near-) uniform/homogeneous chemical composition (Fig.
194 3).

195 *Infrared reflectance spectroscopy*

Near-infrared reflectance spectroscopy measurements of mineral grains in each sample show typical absorption bands of glauconite and nontronite: i) the combination of OH bending plus stretching of adsorbed and interlayered H_2O at ~5246 cm^{-1}, and ii) the combination of OH bending and stretching of octahedral hydroxyls at ~4338-4352 cm^{-1} (vI; see Fig. 4). The position of vI, which is comparable to the range of values reported previously from the same materials (Michalski et al., 2015; Cuadros et al., 2013, 2016, 2019), systematically varies with the cation composition of the octahedral sheets; i.e., ~4348-4352 cm^{-1} for low $(Mg^{2+}+Fe^{2+})_{oct}/M_{oct}$ samples, and ~4338-4345 cm^{-1} for high $(Mg^{2+}+Fe^{2+})_{oct}/M_{oct}$ samples (Table 2; Fig. 4 and 5).

Raman spectroscopy

Raman spectroscopy in the low-wavenumber region reveals two distinctive bands for all samples: v1 ~241-257 cm^{-1} and v2 ~600-606 Δcm^{-1} (Table 2; Fig. 6a). Band v1 is part of a series of bands in the ~250-350 cm^{-1} range, whereas v2 shows a distinctive shoulder/tail at the low-wavenumber side. The positions of v1 and v2 correlate with the composition of the octahedral sheets: i.e., v1 ~241-247 cm^{-1} and v2 ~605-606 cm^{-1} for $(Mg^{2+}+Fe^{2+})_{oct}$-poorer samples; v1 ~254-257 cm^{-1} and v2 ~600-605 cm^{-1} for $(Mg^{2+}+Fe^{2+})_{oct}$-richer samples (Table 2; Fig. 7a and b). Besides v1 and v2, additional bands occur at ~350-550 cm^{-1} and ~690 cm^{-1} (v3); see Fig. 6a. Measurements in the hydroxyl-stretching region show a broad, asymmetric peak (v4). Its position correlates with the chemistry of the octahedral sheets: i.e., v4 ~3568-3570 cm^{-1} and ~3548-3557 cm^{-1} for low and high $(Mg^{2+}+Fe^{2+})_{oct}/M_{oct}$ samples, respectively (Table 2; Fig. 6b and 7c). Analyses of multiple mineral grains in each sample produced similar peak shapes and central positions (Fig. 8), as is consistent with the (near-) uniform/homogeneous chemical compositions of the samples (Fig. 3).

In all samples, the asymmetry of v4, including a shoulder/tail at the high-wavenumber side, allows for its mathematical modelling using three discrete bands: vA, vB and vC (Table

2; Fig. 9). The weak intensity of vC, and its proximity to the other, more intense bands, resulted in more uncertain parameters for this band. Nonetheless, the calculated band centres systematically vary with octahedral composition; i.e., the positions of all three bands are distinctly shifted to lower wavenumber in samples with high $(Mg^{2+}+Fe^{2+})_{oct}/M_{oct}$ (Table 2; Fig. 10a-c). Moreover, covariations exist between the octahedral composition and the other parameters of the assumed bands, including their calculated intensities (A_A/A_B and A_A/A_{tot}, where A_{tot} is the sum of areas of vA, vB and vC) and half-widths at half maximum ($HWHM_A/HWHM_B$); see Table 2 and Fig 10d-f. For example, vA is the dominant band in the spectra of high $(Mg^{2+}\text{-}Fe^{2+})_{oct}/M_{oct}$ samples (high A_A/A_B and high A_A/A_{tot}), whereas vB is dominant in low $(Mg^{2+}\text{-}Fe^{2+})_{oct}/M_{oct}$ samples (low A_A/A_B). The half-widths at half maximum (HWHM) decrease with the prominence of vA and vB; i.e., high $HWHM_A/HWHM_B$ for $(Mg^{2+}\text{-}Fe^{2+})_{oct}$-poorer samples, and comparatively lower $HWHM_A/HWHM_B$ for $(Mg^{2+}\text{-}Fe^{2+})_{oct}$-richer samples.

DISCUSSION

Comparison with previous work

The analyzed nontronite and glauconite-nontronite mixed-layer phases show a series of Raman peaks in the low-wavenumber region (v1, v2, and v3) and hydroxyl stretching domain (v4). These peaks, which are at slightly different positions in each sample (Table 2; Fig 6), were observed in previous studies; see Wang et al. (2015, their figures 10 and 13), and Ospitali et al. (2008, their figure 3). Their assignment is discussed in below. Several additional peaks occur below ~700 cm^{-1}; see Fig. 6a in comparison with data in Ospitali et al. (2008) and Wang et al. (2015). However, their detailed discussion is omitted, because these peaks are insufficiently developed or absent in some of the spectra, due to which eventual origins/influences by trace contaminants not readily observed in SEM images (see Fig. 2b-d) cannot be ruled out.

In this study, v1 (~241-257 cm^{-1}) may relate to the stretching of OH-O bonds in the octahedral sheets [$\nu(OH\text{-}O)_{oct}$]; see Frost and Rintoul (1996a,b). The intensity of this band increases with increasing wavelength of the excitation source; compare Fig. 6a with the glauconite analyses using 514.5 nm, 632.8 nm, and 785 nm lasers in Ospitali et al. (2008, their figure 3). Both v2 and v3, located at ~600-606 cm^{-1} and ~690 cm^{-1}, respectively, likely correspond to Si-O-Si vibrations in the tetrahedral sheets (Wang et al., 2015). The latter band is commonly assigned to the symmetric stretching vibration of Si-O_b-Si [$\nu(Si\text{-}O_b\text{-}Si)_{tet}$], where O_b are oxygen atoms bridging the tetrahedral components (Wang et al., 2015; Kloprogge, 2017). The intensities of both these bands appear to depend on the wavelength of the excitation source. Band v2 is the most intense band in this study, as is consistent with its prominence in the glauconite data acquired using a 514.5 nm laser in Ospitali et al. (2008). The latter study shows that this band is essentially absent in analyses with 632.8 nm and 785 nm lasers, and the same holds true for the analyses of the Hohen-Hagen nontronite standard (NG-1) using a 1064 nm in Frost and Kloprogge (2000a, their figure 2). This difference, which is also observed for v1, could indicate that the transition energy of the relating vibrational mode is not matched by each laser wavelength/frequency. However, this explanation cannot hold true for the weak expression of v3 in this study (Fig. 6a), which contrasts with its strong intensity in the glauconite analyses with a 514.5 nm laser in Ospitali et al. (2008). Although uncertain, this difference could relate to a contrasting polarization configuration of the laser used in Ospitali et al. (2008), and/or an influence by differences in particle size or orientation (compare with Ishibashi et al., 2008, and Foucher et al., 2013).

Finally, there is agreement in the position and intensity of the hydroxyl O-H stretching bands (~3500-3700 cm^{-1} range) for the spectra in this study and those of glauconite and nontronite in the literature; compare Figs 6, 8 and 9 with Wang et al. (2015, their figures 10 and 13). The glauconite spectrum in Wang et al. (2015) shows a broad O-H stretching

band with three maxima; i.e., one peak at ~3600 cm^{-1}, another, more intense peak below 3600 cm^{-1}, and a third peak that accounts for a shoulder on the low wavenumber side of the most intense peak. This composite band is consistent with v4 of the low $(Mg^{2+}+Fe^{2+})_{oct}/M_{oct}$ samples (Figs 6b, 8 and 9a). On the other hand, the nontronite spectrum in Wang et al. (2015) shows an intense peak with a gentle tail on the high-wavenumber side, as is consistent with v4 of the high $(Mg^{2+}+Fe^{2+})_{oct}/M_{oct}$ specimens (Figs 6b, 8 and 9b-c).

Chemistry/structure-dependent Raman spectral features of glauconite and nontronite

For the analyzed nontronite and glauconite-nontronite mixed-layer samples, the covariations between Raman spectral properties and octahedral chemistry (Table 2; Fig. 7 and 10) merits discussion about which chemical and structural properties cause these differences.

Previously, Wang et al. (2015) proposed that a series of spectral features in both the low-wavenumber region and the hydroxyl stretching domain can aid in the discrimination between different phyllosilicate members: i) all phyllosilicates should have their strongest peaks in the 600-800 cm^{-1} range; ii) $\nu(Si\text{-}O_b\text{-}Si)_{tet}$ is below 700 cm^{-1} for trioctahedral species and above 700 cm^{-1} for dioctahedral species, except for Fe-rich dioctahedral phyllosilicates, such as glauconite and nontronite, where it is downshifted to <700 cm^{-1}; iii) Al-rich phyllosilicates have a diagnostic band at ~430 cm^{-1}, Mg-rich phyllosilicates a band at ~350 cm^{-1}, and Fe-rich phyllosilicates a band at ~550-600 cm^{-1}; iv) hydroxyl stretching bands (here v4) of all phyllosilicates appear at >3600 cm^{-1}, except for Fe-rich species (<3600 cm^{-1}). Our data confirm all these propositions; see Table 2 and Figs 6-9.

The data in this study also indicate that the positions of v1, v2, and v4 correlate with the composition of the samples, especially the proportions of divalent and trivalent cations in the octahedral sheets (Fig. 7). The cause for this dependency seems clear for v4: octahedral cations are bound to the OH groups, and thus can influence the frequencies of O-H stretching vibrations; see a more detailed discussion further below. Because OH-stretching vibrations

296 are also active in IR (Fig. 4 and 5), the relating shifts in IR were exploited for the
297 identification of phyllosilicates, such as in surface exploration of Mars (Poulet et al., 2005;
298 Carter et al., 2013; Michalski et al., 2015), and in determination of their octahedral
299 composition and cation order (Bishop et al., 2002a,b; Bishop et al., 2008; Cuadros et al.,
300 2013, 2016, 2019). In Raman spectroscopy, the influence of octahedral composition on v1
301 and v2 cannot be assessed with certainty because the origins of these bands are in part
302 uncertain. To reiterate, v1 may relate to $\nu(OH\text{-}O)_{oct}$ (Frost and Rintoul, 1996a,b), and v2 to
303 $\nu(Si\text{-}O_b\text{-}Si)_{tet}$ (Wang et al., 2015). Provided that this band assignment is correct, the
304 displacement of v1 with chemistry is explainable by the linkage of the octahedral cations to
305 the OH implicated in $\nu(OH\text{-}O)_{oct}$. Although v2 is ascribed to vibration in the tetrahedral
306 sheets, an influence by octahedral chemistry is expectable because octahedral and tetrahedral
307 sheets share O atoms. Consistent with such an indirect influence is the relatively small shift
308 of v2 (~6 cm^{-1}) when compared with that of v1 (~15 cm^{-1}), as well as the lower correlation
309 between octahedral cation occupancy and the position of v2, particularly if compared with
310 that for v1 and v4 (Fig. 7).
311 *Relationship between octahedral cation site occupancy and Raman bands in the hydroxyl*
312 *stretching region*
313 Where vibrations are active in both Raman and IR reflectance spectroscopy, information
314 gathered via the latter technique can aid in detailed interpretation of the Raman bands.
315 Concerning v4 in Raman spectroscopy, the NIR data show a comparable, octahedral cation-
316 sensitive peak corresponding to OH bending and stretching; i.e., vI between ~4338 and
317 ~4352 cm^{-1}, where $(Mg^{2+}+Fe^{2+})_{oct}$-richer samples plot at lower wavenumbers (Table 2; Figs
318 4, 5 and 11). The study of Cuadros et al. (2016) assigned this band shift to overlapping
319 vibration bands of paired metal cation species linked to OH (M-OH-M or M-OH-M'):
320 $AlFe^{3+}OH$, $Fe^{3+}{}_2OH$, $Fe^{3+}MgOH$ $Fe^{3+}Fe^{2+}OH$, and perhaps $Fe^{2+}MgOH$ (Madejová et al.,

1994; Drits et al., 1997; Bishop et al., 2002a,b; Petit et al., 2004). Spectral deconvolution of v4 allows assessing whether its shift is the result of a comparable array of Raman vibrations in such M-OH-M' groups. Whereas peak fitting using three bands (Fig. 9) is not considered to represent each of the potential vibration components of v4 (see further discussion below), it allows exploring whether and how the octahedral cation occupancy influences these assumed bands. Indeed, mathematical modelling indicates that increasing $(Mg^{2+}+Fe^{2+})_{oct}/M_{oct}$ accounts for i) a displacement of the three assumed bands (vA, vB and vC) to lower wavenumbers (Table 2; Fig. 10a-c); ii) an increase in the intensity of vA (Table 2; Fig. 10d-e); iii) a decrease of the width of vA relative to that of vB (Table 2; Fig. 10f).

The causes for the variations among vA, vB and vC can be assessed based on theoretical considerations for hydroxyl stretching modes in phyllosilicates. Theory predicts that the O-H stretching energy of an octahedral OH group, and hence the frequency of the corresponding IR and Raman bands, relates to the strength/length of the O-H bond, which is mainly determined by the cation arrangement and occupancy, and the location/orientation of the OH group (Farmer and Russell, 1964; Farmer, 1968; Rouxhet, 1970; Slonimskaya et al., 1986; Daynyak et al., 1992; Madejová et al., 1994; Besson and Drits, 1997a,b; Drits et al., 1997; Madejová, 2003; Petit et al., 2004; Zviagina et al., 2004; Hofmeister and Bowey, 2006; Wang et al., 2015; Kloprogge, 2017). In trioctahedral phyllosilicates, the vectors of OH groups are oriented perpendicular to the plane of the octahedral sheet, and no H-bondings exist between O and OH. Hence, the weakening of a M-OH bond, such as through the substitution of a large and weakly electronegative cation for a smaller and more electronegative cation (e.g., Mg^{2+} for Fe^{3+}, with radii of ~0.72 Å and 0.65 Å, respectively; Shannon, 1974), is compensated by a strengthening/shortening of the O-H bond, and thus a shift of the O-H stretching vibration to higher wavenumber. However, for dioctahedral glauconite and nontronite, in which the OH vectors are only slightly tilted relative to the octahedral sheets and point towards the cation-

346 vacancies (Fig. 1), the same substitution process accounts for an opposite effect: with
347 increasing $(Mg^{2+}+Fe^{2+})/M_{oct}$, the O-H vibrations are shifted to lower wavenumber. This
348 difference could relate to the presence of cross-vacancy H-bondings between the OH groups
349 and octahedral O atoms in dioctahedral phyllosilicate species (Fig. 1). The substitution of M^{2+}
350 for M^{3+} causes a weakening/lengthening of the M-OH bonds, and thus a
351 strengthening/shortening of the cross-vacancy OH-O bonds, due to which the O-H bonds
352 become weaker and longer, resulting in a downshift of the O-H stretching modes (Besson and
353 Drits 1997b; Drits et al., 1997).

354 Hence, for the analyzed nontronite and glauconite-nontronite phases, the displacement
355 of all the three assumed hydroxyl stretching bands to lower wavenumber with higher
356 $(Mg^{2+}+Fe^{2+})_{oct}/M_{oct}$ can be interpreted in two ways. First, the assumed bands do not
357 correspond to vibrations of a single M-OH-M' group, they encompass vibrations of more
358 than one cation pair. As a result, the bands are displaced as the proportions of cation pairs
359 change. Second, the displacement of the bands relates to an overall change of the M-OH
360 bonding distance in the octahedral sheet; i.e., as the proportion of divalent atoms (mainly
361 Mg^{2+}) increases, the average M-OH distance in the octahedral sheet increases. The second
362 interpretation implies that it is the relative proportion of Fe^{3+} and Mg^{2+} that controls the
363 average M-OH distance in the entire octahedral sheet (note that Fe^{3+} and Mg^{2+} are the most
364 abundant cations, Table 1), with a greater M-OH distance as Mg^{2+} increases, as a result of
365 which all bands are displaced to lower wavenumber. Regardless, the increasing relative area
366 of vA with increasing $(Mg^{2+}+Fe^{2+})_{oct}/M_{oct}$ requires that Mg^{2+} and Fe^{2+} are necessary
367 contributors to this specific band, and that it is a proxy for $(M\text{-}OH\text{-}M')_{oct}$ groups dominated
368 by Mg^{2+} and Fe^{2+} ($Fe^{2+}Mg$, $Fe^{3+}Mg$, $Fe^{3+}Fe^{2+}$, and perhaps also $AlMg$ and $AlFe^{3+}$). The
369 corollary of this interpretation is that vB relates to vibrations involving trivalent cation pairs
370 ($Fe^{3+}{}_2$ and $Fe^{3+}Al$), whereas the presence of vC suggests that the contribution of cation pairs

371 to Raman intensity is complex, with divalent cations mainly contributing to vA and vB (in
372 increasing extent from vB to vA), and trivalent cations contributing to all three bands, in
373 increasing extent from vA to vC. This assignment of assumed hydroxyl bands agrees with the
374 experimental and simulated IR data of 2:1 phyllosilicates in previous studies; see
375 Slonimskaya et al. (1986, their table 2) and Drits et al. (1997, their table 5). These studies
376 show that the positions of the deconvoluted OH-stretching bands are correlated with the
377 cumulative valency of the implicated cation pairs; i.e., OH attached to divalent-divalent
378 cation pairs (e.g., $Mg^{2+}Fe^{2+}$) generally account for O-H stretching vibrations at lower
379 wavenumber if compared with OH attached to divalent-trivalent and trivalent-trivalent cation
380 pairs (e.g., $Mg^{2+}Fe^{3+}$ and $Fe^{3+}{}_2$, respectively).
381 Although the deconvolution of v4 into three separate bands allows for meaningful
382 interpretations, specific results, such as the decreasing width of vA relative to that of vB in
383 parallel to increasing $(Mg^{2+}+Fe^{2+})_{oct}/M_{oct}$ (Fig. 10f), are difficult to interpret. Whereas this
384 variation in band width could indicate that the contribution of OH linked to divalent atoms
385 within the vB envelope is greater than for vA, an artifact from fitting with only three assumed
386 bands cannot be ruled out. To reiterate, this peak likely corresponds to an exceeding number
387 of vibrations of cation pairs linked to OH. Indeed, previous IR studies suggested the likely
388 existence of multiple O-H stretching bands corresponding to the same cation pair (e.g., more
389 than one $Fe_2{}^{3+}OH$ band in glauconite and nontronite), and the same could hold true for
390 Raman spectroscopy. Although the detailed causes for such multiplicities are not entirely
391 understood, factors may be a specific cation occupancy in tetrahedral sheets above and below
392 the octahedral sheet, or modifications in the local octahedral cation environment around a
393 vibrating M-OH-M' group. Even interlayer cations may influence OH stretching modes, as
394 was shown for IR spectra of mica and illite, where K^+ located within the hexagonal cavity of
395 tetrahedral sheets affects the octahedral O-H stretching vibration (Rouxhet, 1970;

Slonimskaya et al., 1986; Besson et al., 1987; Daynyak et al., 1992; Madejová et al., 1994; Besson and Drits, 1997a,b; Drits et al., 1997; Zviagina et al., 2004).

Besides all these uncertainties, the used approximation (3 bands: vA, vB, and vC) sufficiently portrays the theoretically predicted influence of octahedral cation substitution on Raman-active O-H stretching modes, and thus supports the use of the correlation between $(Mg^{2+}+Fe^{2+})_{oct}/M_{oct}$ and the position of v4 as a proxy for octahedral metal occupancy: $M^{2+}{}_{oct}/M_{oct} \sim (v4-3599)/-340$, in which v4 is the wavenumber at the band maximum; $R^2 = 0.87$ (Fig. 7c). However, this calibration is likely only accurate for Mg^{2+}-rich glauconite and nontronite, because in the analyzed samples, the influence of other cation species (e.g., Fe^{2+} and Al^{3+}) on the octahedral domains is limited (Table 1), and thus not assessable.

IMPLICATIONS

The findings in this study have implications for mineral identification and mineral provenance analysis. For example, Raman spectroscopy is an established technique in the characterization of "green earths" used in historic artworks. The study of Ospitali et al. (2008) which compared glauconite from several localities in Italy with that in historic artworks, found differences in Raman spectral features that could be useful for identifying its origin. Indeed, an evaluation of the Raman spectral data in Ospitali et al. (2008, their figure 8) reveals that the glauconite used in some of the examined historic artworks belongs to the low $(Mg^{2+}+Fe^{2+})_{oct}/M_{oct}$ group. Because low Mg^{2+} in glauconite and nontronite is indicative for mineral precipitation at shallow water to continental shelf depositional sites, compared to predominately higher Mg^{2+} incorporation in deep-sea hydrothermal precipitates (Hesse and Schacht 2011), this information can aid in unveiling the historic mining locality for such green earths.

The results in this study will also contribute to the surface exploration of planetary bodies in the solar system, especially Mars. Orbital remote sensing measurements have

provided evidence for the widespread occurrence of (Fe-bearing) phyllosilicates, including glauconite and nontronite, in Mars' Noachian and Hesperian terrains (Poulet et al., 2005; Carter et al., 2013). Future robotic landing missions on Mars will be equipped with Raman spectrometers; i.e., ExoMars of ESA (ESA, 2020), and Perseverance of NASA (NASA, 2020). Hence, the results and interpretations in this study will support the characterization and definitive identification of such phyllosilicates, and hence determination of their provenance and origin on basis of detected crystal structural and chemical properties, as is required for reconstructing the global- to regional-scale paleoenvironmental conditions in Mars' ancient past.

Finally, the structural and chemical characterization of clay minerals through Raman spectroscopy can aid in exploring for economic mineral resources. For example, nontronite, together with saponite, is the principal ore mineral in Ni laterite deposits (Butt & Cluzel, 2013), where these Ni-containing clay species predominately occur in the mid to upper saprolite and pedolith domains developed on ultramafic rocks. Determining the cation composition of these clays down to the lower micron-scale, as feasible by confocal Raman spectroscopy, is important for i) determining the mineralogical hosts of the precious metals, ii) understanding the value of the respective mineral deposit, and iii) driving decisions with regards to ore processing. Furthermore, because nontronite can be diagnostic for alteration of ferromagnesian rocks, the adoption of cost-effective Raman spectroscopy for its chemical and structural characterization can support the exploration for other greenstone-hosted ore deposits, such as the gold deposits in the Yilgarn Craton of Western Australia; e.g. Bronzewing deposit (Cudahy et al., 1995).

CONCLUSIONS

In this study, Raman spectroscopy analysis of nontronite and glauconite-nontronite mixed-layer phases from deep sea hydrothermal fields reveals that these phyllosilicates have

446 diagnostic Raman spectral features that include a series of strong peaks in the low-wavenumber
447 region (<700 cm^{-1}) and the hydroxyl domain (3500-3700 cm^{-1}).

448 Specifically, we have identified three diagnostic peaks in the low wavenumber region:
449 i) v1 ~241-257 cm^{-1}; ii) v2 ~600-606 cm^{-1}; ii) v3 ~690 cm^{-1}. Peak v1, which presumably
450 corresponds to OH-O formed from O of tetrahedral sheets and OH octahedral sheets, is shifted
451 to a higher wavenumber with increasing M^{2+}_{oct}/M_{oct}, whereas v2, which relates to Si-O_b-Si
452 vibrations in the tetrahedral sheets, shows an inverse (negative) relationship between
453 M^{2+}_{oct}/M_{oct} and wavenumber. Moreover, a strong correlation between $(Mg^{2+}+Fe^{2+})_{oct}/M_{oct}$ and
454 the position of the hydroxyl stretching band (v4 ~3548-3570 cm^{-1}) allows to propose for both
455 the high and low $(Mg^{2+}+Fe^{2+})_{oct}/M_{oct}$ samples a simplified calibration model for the octahedral
456 cation occupancy: M^{2+}_{oct}/M_{oct} ~ (v4-3603)/-333 (Fig. 7c), in which v4 is the wavenumber at
457 the band maximum (see Fig. 8).

458 Taken together, our study shows that Raman spectroscopy can be used for the rapid and
459 reliable characterization of glauconite, nontronite, and glauconite-nontronite mixed layer
460 phases, which is particularly important for mineral characterization and mineral provenance
461 analysis by Raman spectroscopic analysis on Earth and during robotic surface exploration of
462 planets elsewhere in the solar system, especially Mars, where phyllosilicates with a wide range
463 of Al-Mg-Fe^{2+}-Fe^{3+} composition occur.

464 **ACKNOWLEDGMENTS**

465 The authors acknowledge the facilities, and the scientific and technical assistance of the
466 Australian Microscopy & Microanalysis Research Facility at Centre for Microscopy,
467 Characterization and Analysis (UWA). We thank Hongwu Xu and Janice Bishop for their
468 editorial handling, and two anonymous reviewers for their constructive comments. Derek

Winchester and Adam Ramage (both CSIRO Kensington, Perth) are thanked for their help with sample preparation.

REFERENCES

Bersani, D., Vignola, S.A.P., Moltifiori, G., Marino, I.G., Lottici, P.P., and Diella, V. (2009) Micro-Raman spectroscopy as a routine tool for garnet analysis. Spectrochimica Acta, Part A: Molecular and Biomolecular Spectroscopy, 73, 484-491.

Besson, G., and Drits, V.A. (1997a) Refined relationships between chemical composition of dioctahedral fine-grained mica minerals and their infrared spectra within the OH stretching region. Part I: Identification of the OH stretching bands. Clays and Clay Minerals, 45, 158-69.

Besson, G., and Drits, V.A. (1997b) Refined relationships between chemical composition of dioctahedral fine-grained micaceous minerals and their infrared spectra within the OH stretching region. Part II: The main factors affecting OH vibrations and quantitative analysis. Clays and Clay Minerals, 45, 170-183.

Besson, G., Drits, V., Daynyak, L. and Somaliar, B. (1987) Analysis of cation distribution in dioctahedral micaceous minerals on the basis of IR spectroscopy data. Clay Minerals, 22, 465-478.

Bishop J., Madejová J., Komadel P., and Fröschl H. (2002a) The influence of structural Fe, Al and Mg on the infrared OH bands in spectra of dioctahedral smectites. Clay Minerals, 37, 607-616.

Bishop J., Murad E., Dyar M. (2002b) The influence of octahedral and tetrahedral cation substitution on the structure of smectites and serpentines as observed through infrared spectroscopy. Clay Minerals, 37, 617-628.

Bishop, J.L., Lane, M.D., Dyar, M.D., and Brown, A.J. (2008) Reflectance and emission spectroscopy study of four groups of phyllosilicates: smectites, kaolinite-serpentines, chlorites and micas. Clay Minerals, 43, 35-54.

493 Blaha, J.J., and Rosasco, G.J. (1978) Raman microprobe spectra of individual microcrystals and fibers
494 of talc, tremolite, and related silicate minerals Analytical Chemistry, 50, 892-896.

495 Butt, C.R., and Cluzel, D. (2013) Nickel laterite deposits: Weathered serpentinites. Elements, 9, 123-
496 128.

497 Carter, J., Poulet, F., Bibring, J.P., Mangold, N., and Murchie, S. (2013) Hydrous minerals on Mars as
498 seen by CRISM and OMEGA imaging spectrometers: updated global view. Journal of
499 Geophysical Research, 118, 831-858.

500 Cuadros, J., Michalski, J.R., Dekov, V., and Bishop, J.L. (2016) Octahedral chemistry of 2:1 clay
501 minerals and hydroxyl band position in the near-infrared: Application to Mars. American
502 Mineralogist, 101, 554-563.

503 Cuadros, J., Michalski, J.R., Dekov, V., Bishop, J., Fiore, S., and Dyar, M.D. (2013) Crystal-
504 chemistry of interstratified Mg/Fe-clay minerals from seafloor hydrothermal sites. Chemical
505 Geology, 360-361, 142-158.

506 Cuadros, J., Michalski, J.R., Dyar, M.D., and Dekov, V. (2019) Controls on tetrahedral Fe(III)
507 abundance in 2:1 phyllosilicates. American Mineralogist, 104, 1608-1619.

508 Cudahy, T.J., Gray, D., Phillips, R.N., and Wildman, J. (1995) Pilot spectral study of the Bronzewing
509 Gold Deposit, Western Australia, 106 p., CSIRO Exploration and Mining Report 124r.

510 Daynyak, L., Drits, V.A., and Heifits, L.M. (1992) Computer simulation of cations distribution in
511 dioctahedral 2:1 layer silicates using IR-data: application to Mössbauer spectroscopy of a
512 glauconite sample. Clays and Clay Minerals, 40, 470-479.

513 Daynyak, L., Drits, V.D. (1987) Interpretation of Mössbauer spectra of nontronite, celadonite, and
514 glauconite. Clays, and Clay Minerals, 35, 363-372.

515 Drits, V., Daynyak, L., Muller, F., Besson, G., and Manceau, A. (1997) Isomorphous cation
516 distribution in celadonites, glauconites and Fe-illites determined by infrared, Mösbauer and
517 EXAFS spectroscopies. Clay Minerals, 32, 153-179.

European Space Agency (accessed 12/10/20). Robotic exploration of Mars. https://exploration.esa.int/web/mars/-/45103-rover-instruments?fbodylongid=2130.

Farmer, V.C. (1968) Infrared spectroscopy in clay mineral studies. Clay Minerals, 7, 373-387.

Farmer, V.C., and Russell, J.D. (1964) The infra-red spectra of layer silicates. Spectrochimica Acta, 20, 1149-1173.

Foucher, F., Lopez-Reyes, G., Bost, N., Rull-Perez, F., Rüßmann, P., Westall, F. (2013) Effect of grain size distribution on Raman analyses and the consequences for in situ planetary missions. Journal of Raman Spectroscopy, 44, 916-925.

Frost, R.L., and Kloprogge, J.T. (2000a) Raman spectroscopy of nontronites. Applied Spectroscopy, 54, 402-405.

Frost, R.L., and Kloprogger, J.T. (2000b) Vibrational spectroscopy of ferruginous smectite and nontronite. Spectrochimica Acta Part A, 56, 2177-2189.

Frost, R.L., and Rintoul, L. (1996a) FT Raman spectroscopy of montmorillonites. International Ceramic Monographs, 2, 325-331.

Frost, R.L., and Rintoul, L. (1996b) Lattice vibrations of montmorillonite: an FT Raman and X-ray diffraction study. Applied Clay Science, 11, 171-183.

Griffiths, W.P. (1969) Raman spectroscopy of minerals. Nature, 224, 264-266.

Hesse, R., and Schacht, U. (2011) Early diagenesis of deep-sea sediments. In H. Hüneke, and T. Mudler, Eds., Deep-Sea Sediments, Developments in Sedimentology, 63, p. 557-713. Elsevier, Amsterdam.

Hofmeister, A.M., and Bowey, J.E. (2006) Quantitative infrared spectra of hydrosilicates and related minerals. Monthly Notices of the Royal Astronomical Society, 367, 577-591.

Ishibashi, H., Arakawa, M., Ohi, S., Yamamoto, J., Miyake, A., Kagi, H. (2008) Relationship between Raman spectral pattern and crystallographic orientation of a rock-forming mineral: a case study of $Fo_{89}Fa_{11}$ olivine. Journal of Raman Spectroscopy, 39, 1653-1659.

543 Kloprogge, J.T. (2017) Raman spectroscopy of clay minerals. In W.P. Gates., J.T. Kloprogge, J.
544 Madejová, and F. Bergaya, Eds., Infrared and Raman Spectroscopies of Clay Minerals, p. 150-
545 199. Elsevier, Amsterdam.

546 Kuebler, K.E., Jolliff, B.L., Wang, A., and Haskin, L.A. (2006) Extracting olivine (Fo–Fa)
547 compositions from Raman spectral peak positions. Geochimica et Cosmochimica Acta, 70, 6201-
548 6222.

549 Madejová, J. (2003) FTIR techniques in clay mineral studies. Vibrational Spectroscopy, 31, 1-10.

550 Madejová, J., Komadel, P., and Čičel, B. (1994) Infrared study of octahedral site populations in
551 smectites. Clay Minerals, 29, 319-326.

552 McMillan, P.F. (1989) Raman spectroscopy in mineralogy and geochemistry. Annual Review of Earth
553 and Planetary Sciences, 17, 255-283.

554 Michaelian, K.H. (1986) The Raman spectrum of kaolinite #9 at 21°C. Canadian Journal of
555 Chemistry, 64, 285-289.

556 Michalski, J.R., Cuadros, J., Bishop, J.L., Dyar, M.D., Dekov, V., and Fiore, S. (2015) Constraints on
557 the crystal-chemistry of Fe/Mg-rich smectitic clays on Mars and links to global alteration trends.
558 Earth and Planetary Science Letters, 42, 215-225.

559 North American Space Agency (accessed 12/10/20). Mars 2020 Mission Perseverance Rover.
560 https://mars.nasa.gov/mars2020/spacecraft/instruments/.

561 Ospitali, F., Bersano, D., Di Lonardo, G., and Lottici, P.P. (2008) 'Green earths': vibrational and
562 elemental characterization of glauconites, celadonites and historical pigments. Journal of Raman
563 Spectroscopy, 39, 1066-1073.

564 Petit, S., Decarreau, A., Martin, F., and Buchet, R. (2004) Refined relationship between the position
565 of the fundamental OH stretching and the first overtones for clays. Physics and Chemistry of
566 Minerals, 31, 585-592.

Poulet, F., Bibring, J.P., Mustard, J.F., Gendrin, A., Mangold, N., Langevin, Y., Arvidson, R.E., Gondet, B., Gomez, C., and The Omega Team (2005) Phyllosilicates on Mars and implications for early martian climate. Nature, 438, 623-627.

Rouxhet, P. (1970) Hydroxyl stretching bands in micas: a quantitative interpretation. Clay Minerals, 8, 375-378.

Shannon, R.D. (1976) Revised Effective Ionic Radii and Systematic Studies of Interatomie Distances in Halides and Chaleogenides. Acta Crystallographica Section A, 32, 751-767.

Slonimskaya, M., Besson, G., Daynyak, L., Tchoubar, C., and Drits, V. (1986) Interpretation of the IR spectra of celadonites and glauconites in the region of OH-stretching frequencies. Clay Minerals, 21, 377-388.

Tlili, A., Smith, D.C., Beny, J.M., and Boyer, H. (1989) A Raman microprobe study of natural micas. Mineralogical Magazine, 53, 165-179.

Wang, A., Freeman, J.J., and Jolliff, B.L. (2015) Understanding the Raman spectral features of phyllosilicates. Journal of Raman Spectroscopy, 46, 829-845.

Wang, A., Jolliff, B.L., Haskin, L.A., Kuebler, K.E., and Viskupic, K.M. (2001) Characterization and comparison of structural and compositional features of planetary quadrilateral pyroxenes by Raman spectroscopy. American Mineralogist, 86, 790-806.

Zviagina, B.B., McCarthy, D.K., Srodon, J., and Drits, V.A. (2004) Interpretation of infrared spectra of dioctahedral smectites in the region of OH-stretching vibrations. Clays and Clay Minerals, 53, 399-410.

This is the peer-reviewed, final accepted version for American Mineralogist, published by the Mineralogical Society of America.
The published version is subject to change. Cite as Authors (Year) Title. American Mineralogist, in press.
DOI: https://doi.org/10.2138/am-2022-8044. http://www.minsocam.org/

TABLES

Table 1 Sampling locations and chemistry of analyzed glauconite-nontronite samples. Data are from Cuadros et al. (2013).

Sample	Locality	G:N	Si	Al_{tet}	Fe_{tet}	Al_{oct}	Mg_{oct}	Fe^{3+}	Fe^{2+}	Mn	Ti	Mg	Ca	Na	K	M_{oct}	Charge
Low $(Fe^{2+}+Mg^{2+})_{oct}/M_{oct}$																	
Va22-146KS-639-640	Atlantis II Deep, Red Sea	33:77	3.62	0.00	0.38	0.00	0.23	1.84	0.00	0.00	0.00	0.00	0.05	0.00	0.28	2.08	-0.0006
Va22-146KS-612-614	Atlantis II Deep, Red Sea	59:41	3.68	0.09	0.23	0.02	0.20	1.79	0.00	0.00	0.00	0.00	0.09	0.00	0.27	2.02	-0.0003
Va22-146 KS-603-604	Atlantis II Deep, Red Sea	50:50	3.74	0.04	0.22	0.03	0.18	1.79	0.00	0.00	0.00	0.00	0.06	0.00	0.33	2.00	-0.0003
Va22-146KS-588-591	Atlantis II Deep, Red Sea	56:44	3.73	0.00	0.27	0.05	0.17	1.73	0.04	0.00	0.00	0.00	0.09	0.00	0.35	1.99	-0.0002
High $(Fe^{2+}+Mg^{2+})_{oct}/M_{oct}$																	
Va22-146KS-1030-1034	Atlantis II Deep, Red Sea	23:77	3.80	0.02	0.18	0.06	0.17	1.58	0.11	0.05	0.00	0.00	0.04	0.03	0.49	1.98	-0.0004
Cy 82-14-5	East Pacific Rise	100:0	3.60	0.04	0.36	0.00	0.28	1.76	0.00	0.00	0.00	0.00	0.03	0.48	0.03	2.04	0.0000
1183-15	East Pacific Rise	100:0	3.62	0.01	0.37	0.00	0.31	1.67	0.00	0.01	0.00	0.00	0.00	0.40	0.31	1.99	0.0000
Va22-146 KS-1145-1146	Atlantis II Deep, Red Sea	47:53	3.95	0.05	0.00	0.04	0.25	1.65	0.05	0.00	0.00	0.00	0.01	0.11	0.24	1.99	-0.0007
Va22-146KS-1144-1145	Atlantis II Deep, Red Sea	68:32	3.93	0.05	0.02	0.00	0.25	1.69	0.05	0.00	0.00	0.00	0.00	0.12	0.25	2.00	-0.0005

G:N = proportion of glauconite and nontronite layers; M_{oct} = sum of metal cations in the octahedral sheets.

This is the peer-reviewed, final accepted version for American Mineralogist, published by the Mineralogical Society of America.
The published version is subject to change. Cite as Authors (Year) Title. American Mineralogist, in press.
DOI: https://doi.org/10.2138/am-2022-8044. http://www.minsocam.org/

Table 2 Summary of near-infrared (NIR) and Raman spectroscopic features of analyzed glauconite-nontronite samples.

Sample	Mineralogy/chemistry		Near-infrared spectroscopy	Raman spectroscopy								
	G:N	$(Mg^{2+}+Fe^{2+})_{oct}/M_{oct}$	vI cm^{-1}	v1 cm^{-1}	v2 cm^{-1}	v4 cm^{-1}	vA cm^{-1}	vB cm^{-1}	vC cm^{-1}	$HWHM_A/HWHM_B$	A_A/A_B	A_A/A_{tot}
Low $(Fe^{2+}+Mg^{2+})_{oct}/M_{oct}$												
Va22-146KS-639-640	33:77	0.11	4352.4	241.4	605.7	3569.2	3541.8	3572.5	3610.2	1.34	1.24	0.42
Va22-146KS-612-614	59:41	0.10	4350.2	242.2	605.5	3570.2	3541.7	3571.9	3608.9	1.42	1.21	0.41
Va22-146 KS-603-604	50:50	0.09	4349.1	241.9	604.6	3568.4	3540.6	3571.2	3608.3	1.36	1.36	0.45
Va22-146KS-588-591	56:44	0.11	4347.7	246.5	606.2	3569.8	3541.8	3572.3	3608.8	1.39	1.35	0.41
High $(Fe^{2+}+Mg^{2+})_{oct}/M_{oct}$												
Va22-146KS-1030-1034	23:77	0.14	4339.4	253.6	604.5	3555.7	3538.2	3567.6	3606.3	1.16	1.50	0.47
Cy 82-14-5	100:0	0.14	4345.1	254.8	601.3	3557.1	3540.4	3566.4	3607.3	1.20	1.61	0.44
1183-15	100:0	0.16	4343.9	256.8	601.8	3555.4	3539.0	3566.5	3605.3	1.07	1.56	0.50
Va22-146 KS-1145-1146	47:53	0.15	4338.4	254.9	599.9	3548.2	3539.5	3562.6	3604.9	0.97	1.72	0.49
Va22-146KS-1144-1145	68:32	0.15	4338.3	255.4	602.8	3549.6	3538.3	3560.3	3604.3	1.05	1.67	0.48

See main text for assignment of NIR and Raman bands. A_{tot} = Total area of vA, vB, and vC; HWHM = half width at half maximum; G:N = proportion of glauconite and nontronite layers.

FIGURES

Fig. 1 (*1/2 page width in final manuscript*) Fragment of a dioctahedral sheet of 2:1 phyllosilicates. The sketch exemplarily shows a trans-vacant dioctahedral sheet, perhaps the predominate cation configuration of Fe^{3+}-rich 2:1 phyllosilicates (see discussion in Drits and Besson, 1997b), in which the OH groups belong to mirrored cis-octahedrons (C1, C2). Red in the schematic diagram denotes the potential configuration of hydrogen bonds across a cation-vacant trans-octahedron (T). Indicated in inset is the low inclination of the O-H vectors relative to the plane of the octahedral sheet (compare with Daynyak and Drits, 1987).

Fig. 2 (*2/3 page width in final manuscript*) Scanning Electron Microscopy images of purified nontronite and glauconite-nontronite mixed-layer samples from hydrothermal fields of the Atlantis II Deep and the East Pacific Ridge; compare with Table 1. (a) Secondary electron (SE) and backscattered electron (BSE; inset) images of a nontronite grain in sample 1183-15. (b-d) BSE images showing the micromineralogy in samples 1183-15 and Va22-146KS-588-591. Note the partially crackled, sheath- to rope-like habit of particles (compare with inset in a). Red arrows indicate relict Cu-rich oxide and/or Fe-hydroxide grains (determined by EDS analysis; not shown herein) that can be readily distinguished in BSE imagery owing to their high brightness. (e-h) BSE images (e, g and h) and SE image (f) of stacked or detached and tortuous, platy to fibrous nontronite and glauconite-nontronite particles.

Fig. 3 (*2/3 page width in final manuscript*) Backscattered electron images (a and c) and corresponding EDS analyses (b and d) of grains from samples Va22-146KS-612-614 and 1183-15. The rectangles in the BSE images (a and c) indicate the sites of EDS elemental analyses. Elements are identified on basis of Kα and Kβ X-ray emission lines. Sodium is mostly contamination from $NaHCO_3$ treatment during sample preparation (see Cuadros et al., 2013). The unusually high Si and O peaks likely relate to signal counts from the glass slides to which the glauconite-nontronite grains were attached through adhesive tape (see Methods). Note in each sample the relatively invariant chemical composition of mineral grains. White arrows in c indicate Fe-hydroxide and/or Cu-rich grains.

Fig. 4 (*1/2 page width in final manuscript*) Extended near-infrared (NIR) reflectance spectra of the nontronite and glauconite-nontronite mixed-layer samples (see Table 1). The spectral feature of interest is the peak at ~4338-4352 cm^{-1} (vI), which is assigned to the combination of OH bending and stretching vibrations of hydroxyl groups in the octahedral sheets. The grey area marks the range of its position. The other band at ~5246 cm^{-1} is the combination of OH bending and stretching vibrations of H_2O adsorbed onto the surface and interlayer spaces of the phyllosilicates.

Fig. 5 (*1/2 page width in final manuscript*) Diagram for the ratio between divalent and total cations in octahedral sheets [$(Mg^{2+}+Fe^{2+})/M_{oct}$, where M_{oct} = sum of octahedral cations ($Fe^{3+}+Al^{3+}+Mg^{2+}+Fe^{2+}$)] versus the position of the band combination of O-H stretching and bending (vI; compare with Fig. 4 and see Table 2). Samples are discriminated into high and low $(Mg^{2+}+Fe^{2+})_{oct}/M_{oct}$.

Fig. 6 (*2/3 page width in final manuscript*) Raman spectra of samples in the low-wavenumber region (a) and the hydroxyl stretching region (b). Three peaks in the low-wavenumber region (v1, v2 and v3), and one in the hydroxyl stretching region (v4) are marked. The grey areas mark the range of band positions of v1, v2 and v4. Additional weak Raman bands of uncertain origin are indicated in (a).

Fig. 7 (*2/3 page width in final manuscript*) Diagram for the ratio between divalent and total cations in octahedral sheets [$(Mg^{2+}+Fe^{2+})/M_{oct}$, where M_{oct} is sum of octahedral cations ($Fe^{3+}+Al^{3+}+Mg^{2+}+Fe^{2+}$)] versus the Raman band positions in the low-wavenumber region (v1 and v2 in a and b, respectively) and the hydroxyl-stretching region (v4 in c). Samples are discriminated into high and low $(Mg^{2+}+Fe^{2+})_{oct}/M_{oct}$.

Fig. 8 (*1/2 page width in final manuscript*) Raman spectra of the hydroxyl region of grains in glauconite-nontronite Va22-146KS-603-694 (Atlantis II Deep) and nontronite 1183-15 (East Pacific Rise). For $(Mg^{2+}+Fe^{2+})$-richer sample 1183-15, v4 is shifted to lower frequencies than $(Mg^{2+}+Fe^{2+})$-poorer sample Va22-146KS-603-604. Note the limited variability of spectral features in each sample.

Fig. 9 (*1/2 page width in final manuscript*) Raman spectra of the hydroxyl-stretching region from samples Va22-146KS-603-604, Va22-146KS-1030-1040 and 1183-15. Fitting of spectra using

Gaussian peak functions indicates the presence of three bands (vA, vB and vC), whose positions and intensities are controlled by the octahedral composition of the glauconite-nontronite specimens.

Fig. 10 (*1/2 page width in final manuscript*) Diagrams for the ratio between divalent and total cations in octahedral sheets [$(Mg^{2+}+Fe^{2+})/M_{oct}$, where M_{oct} is sum of octahedral cations $(Fe^{3+}+Al^{3+}+Mg^{2+}+Fe^{2+})$] versus the calculated parameters of the assumed components in v4: i) positions of vA, vB and vC (a-c); ii) ratio between the areas of vA and vB (d); iii) ratio between the areas of vA and v4 (e); iv) ratio of half width at half maximum of components vA and vB (f). Samples are discriminated into high and low $(Mg^{2+}+Fe^{2+})_{oct}/M_{oct}$.

Fig. 11 (*1/2 page width in final manuscript*) Plot of the combination of hydroxyl stretching and bending vibration modes in NIR versus stretching vibration modes in Raman spectroscopy. Samples are discriminated into high and low $(Mg^{2+}+Fe^{2+})_{oct}/M_{oct}$.

Fig. 1

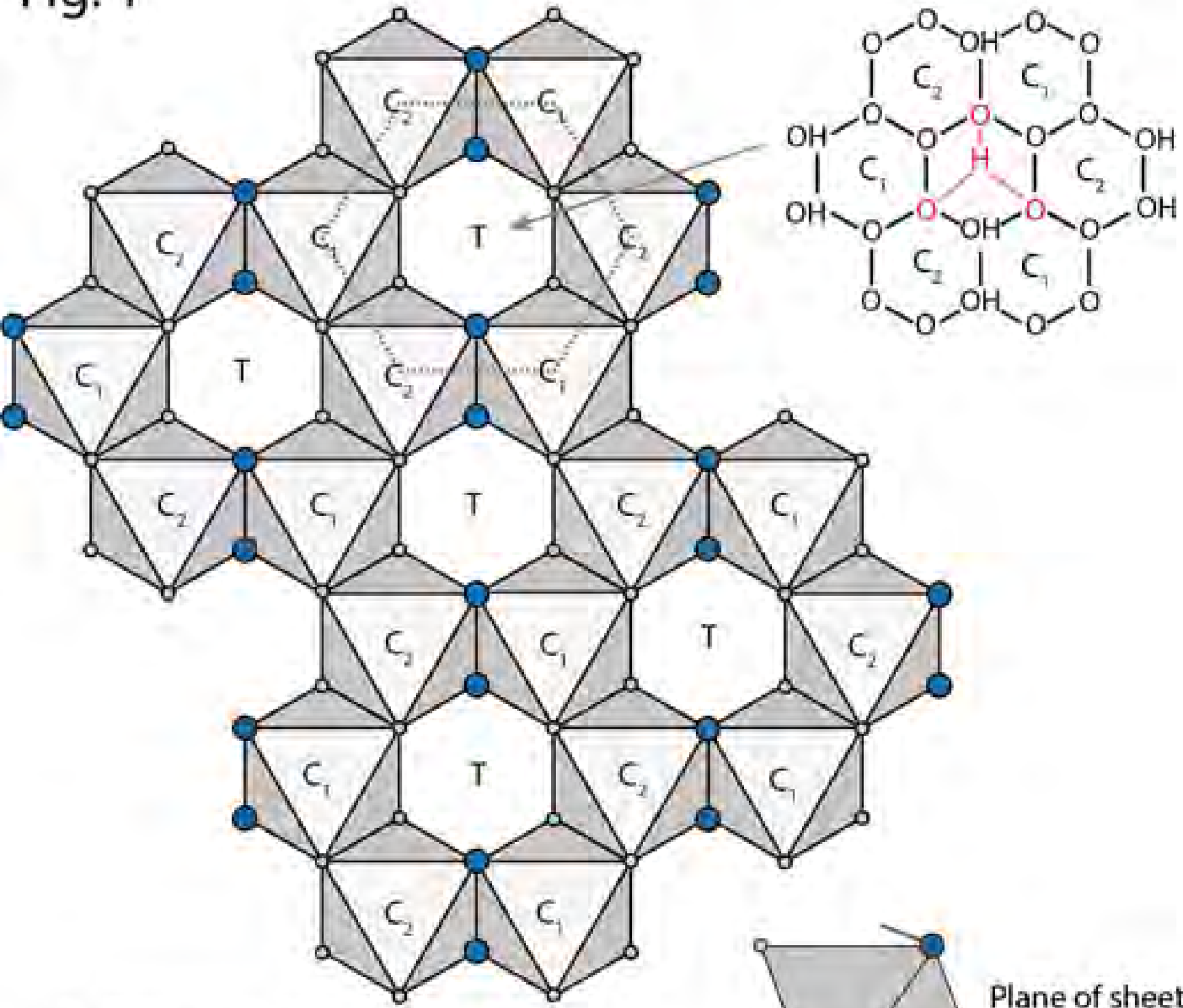

T Cation-vacant trans-octahedron

C1,C2 Cation-occupied cis-octahedron

Hydroxyl group (OH)

Oxygen (O)

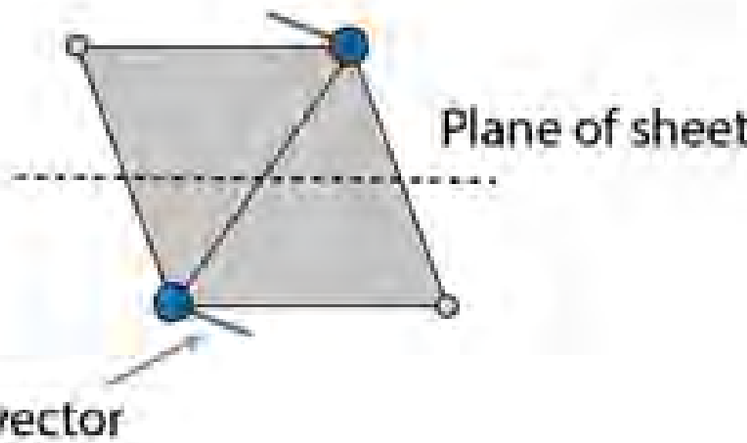

Fig. 2

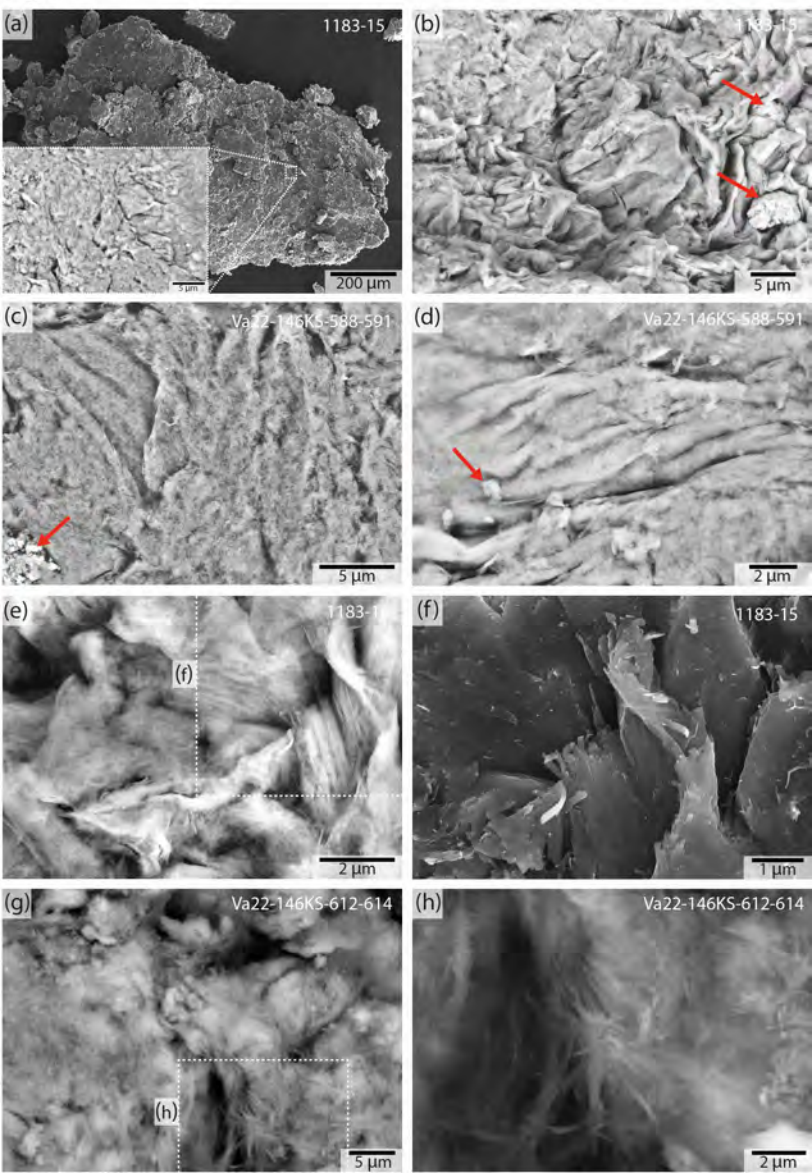
(a)
1183-15
5 µm
200 µm
(b)
1183-15
5 µm
(c)
Va22-146KS-588-591
5 µm
(d)
Va22-146KS-588-591
2 µm
(e)
1183-15
(f)
2 µm
(f)
1183-15
1 µm
(g)
Va22-146KS-612-614
(h)
5 µm
(h)
Va22-146KS-612-614
2 µm

Fig. 3

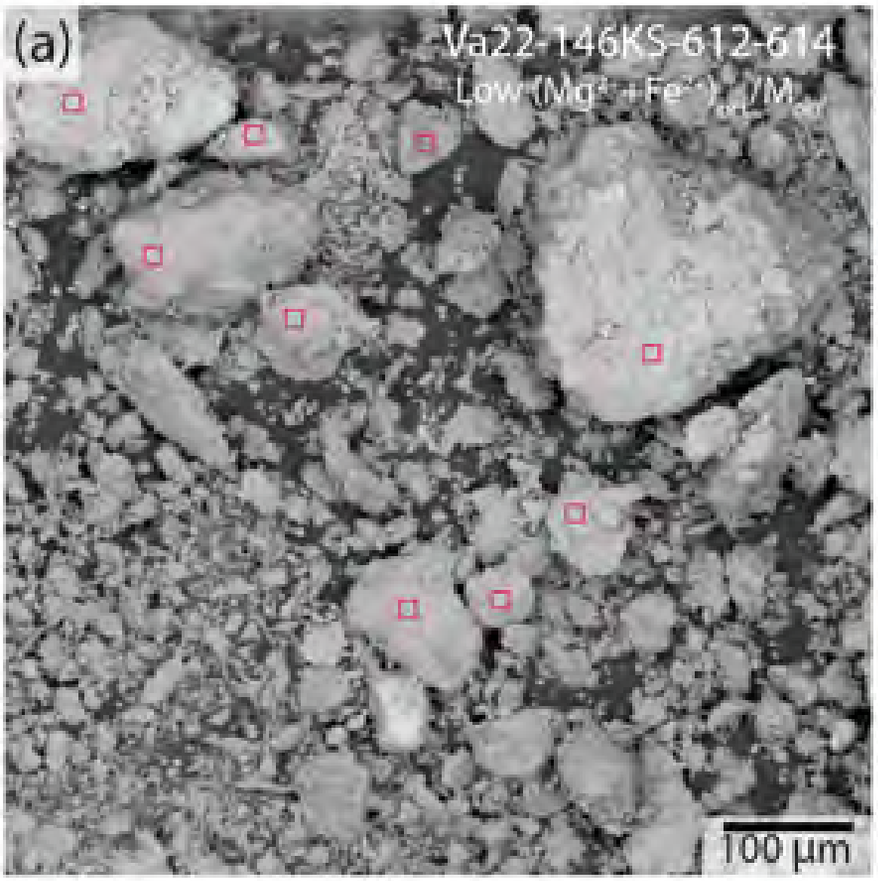
(a)
Va22-146KS-612-614
100 µm

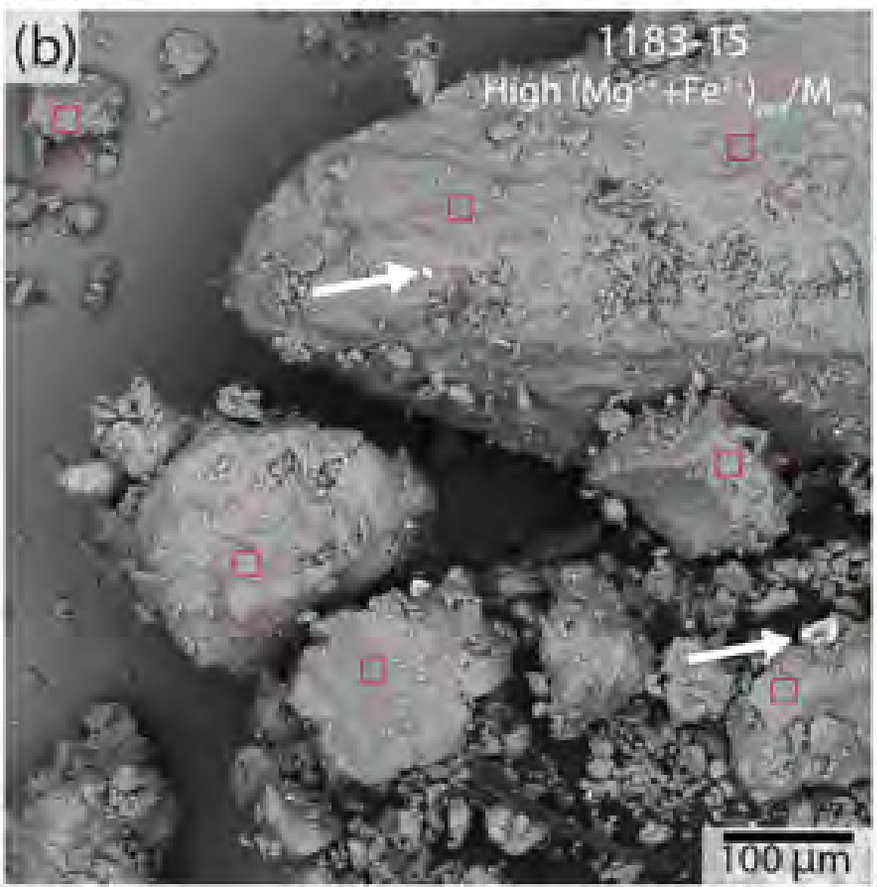
(b)
1183-TS
100 µm

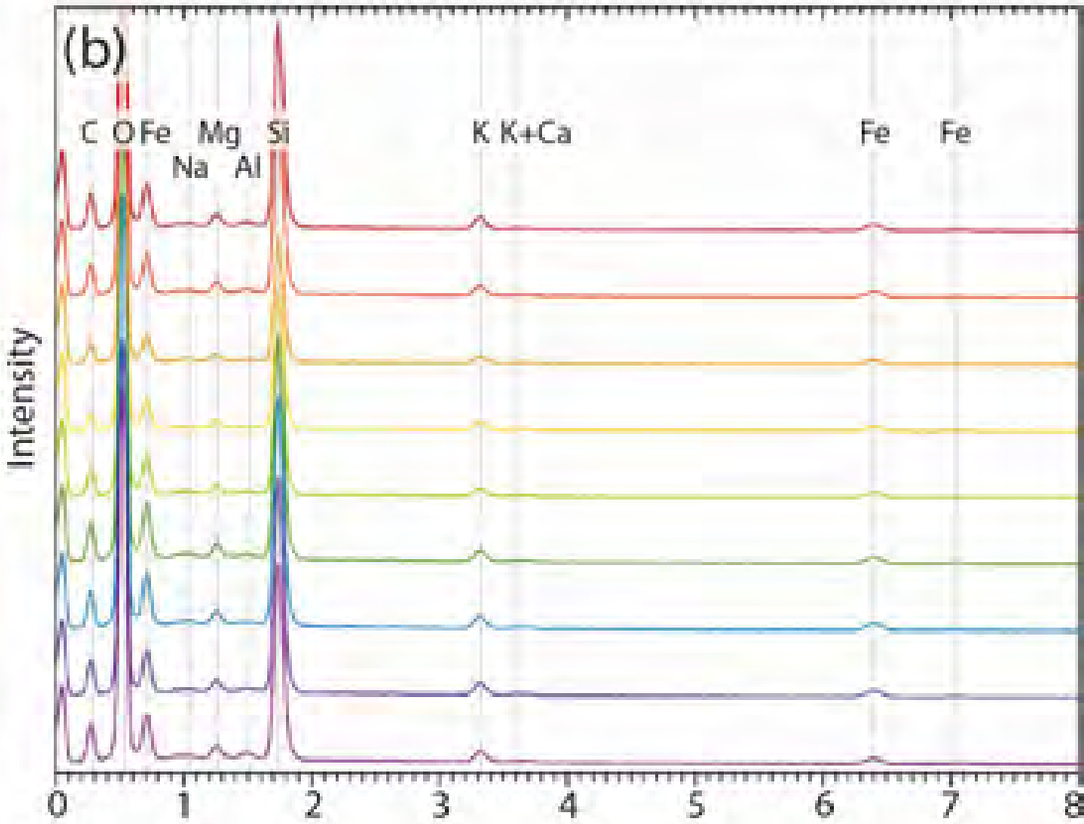
(b)
C O Fe Mg Si
Na Al
K K+Ca
Fe Fe
Intensity
0 1 2 3 4 5 6 7 8

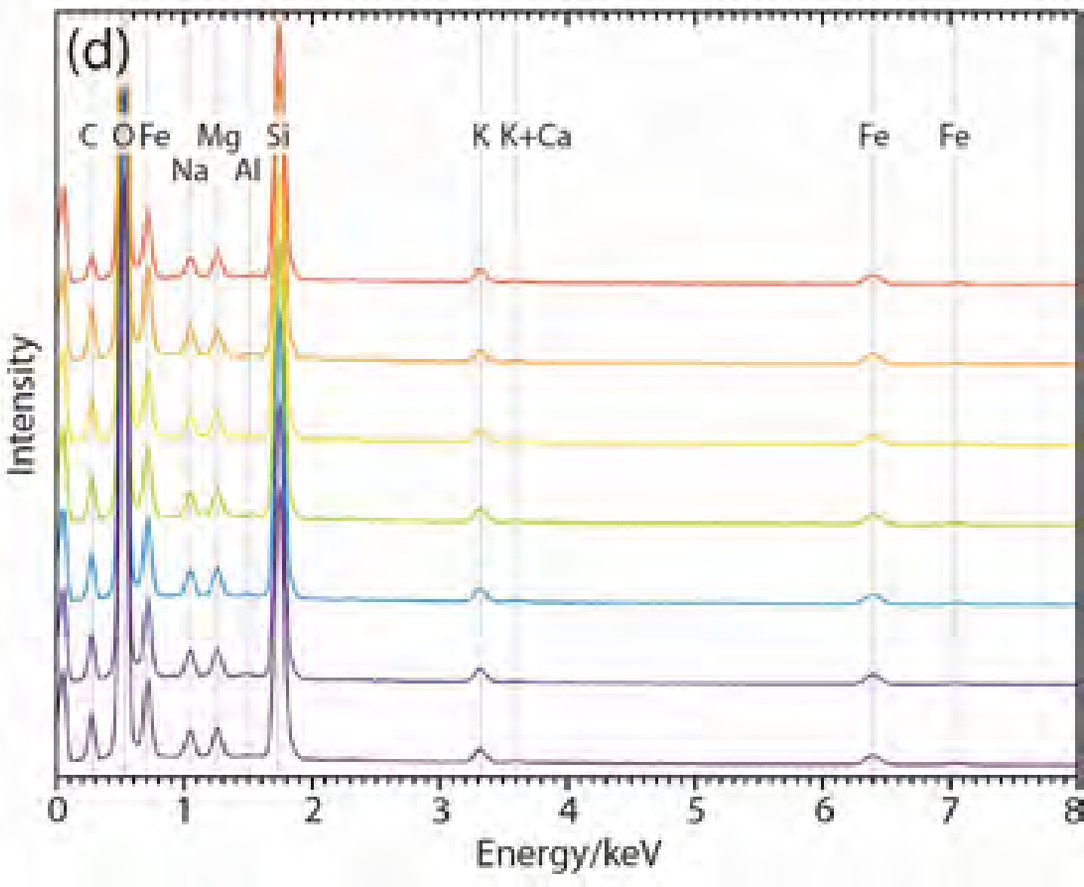
(d)
C O Fe Mg Si
Na Al
K K+Ca
Fe Fe
Intensity
0 1 2 3 4 5 6 7 8
Energy/keV

Fig. 4

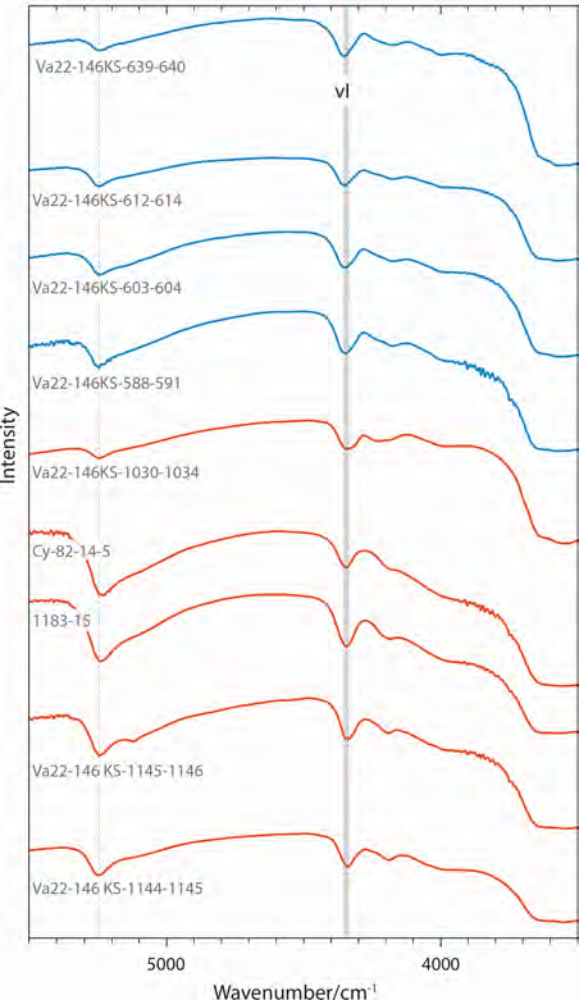
Va22-146KS-639-640
vl
Va22-146KS-612-614
Va22-146KS-603-604
Va22-146KS-588-591
Va22-146KS-1030-1034
Cy-82-14-5
1183-15
Va22-146 KS-1145-1146
Va22-146 KS-1144-1145
Intensity
5000
4000
Wavenumber/cm-1

Fig. 5

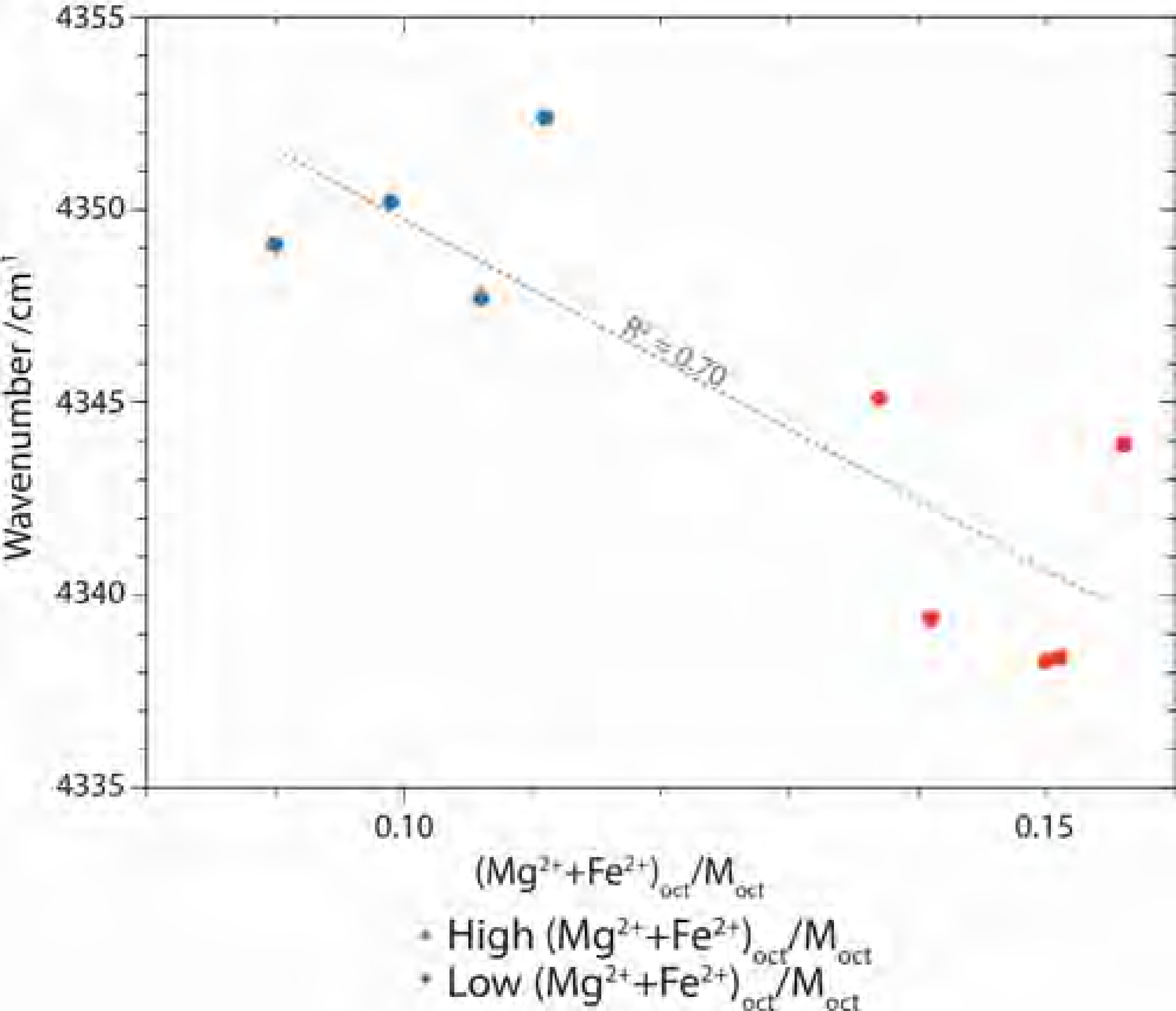
4355
4350
4345
4340
4335
Wavenumber /cm-1
R² = 0.70
0.10
0.15
(Mg2++Fe2+)oct/Moct
High (Mg2++Fe2+)oct/Moct
Low (Mg2++Fe2+)oct/Moct

Fig. 6

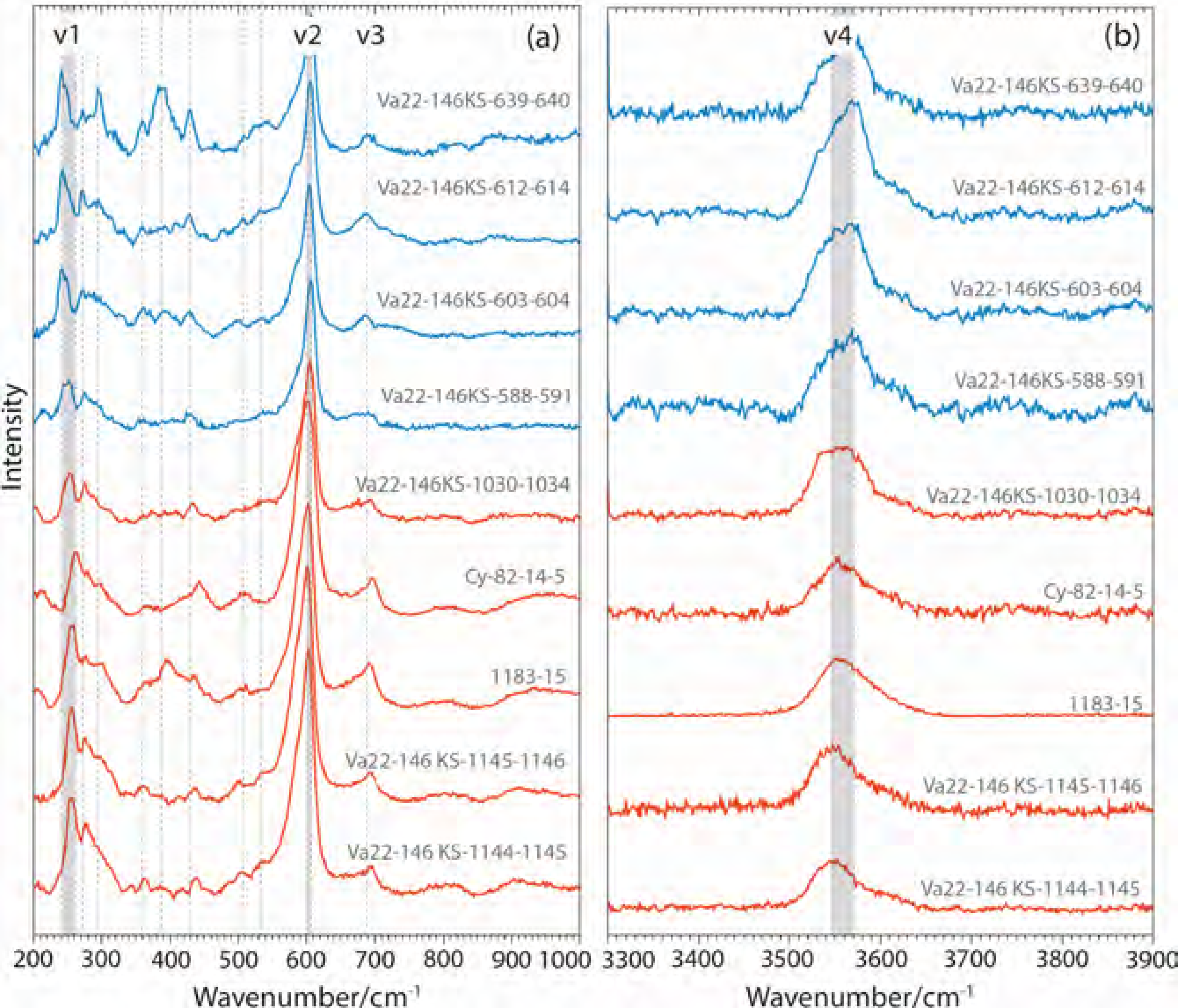
v1
v2
v3
(a)
v4
(b)
Va22-146KS-639-640
Va22-146KS-612-614
Va22-146KS-603-604
Va22-146KS-588-591
Va22-146KS-1030-1034
Cy-82-14-5
1183-15
Va22-146 KS-1145-1146
Va22-146 KS-1144-1145
Intensity
200 300 400 500 600 700 800 900 1000
Wavenumber/cm-1
3300 3400 3500 3600 3700 3800 3900
Wavenumber/cm-1

Fig. 7

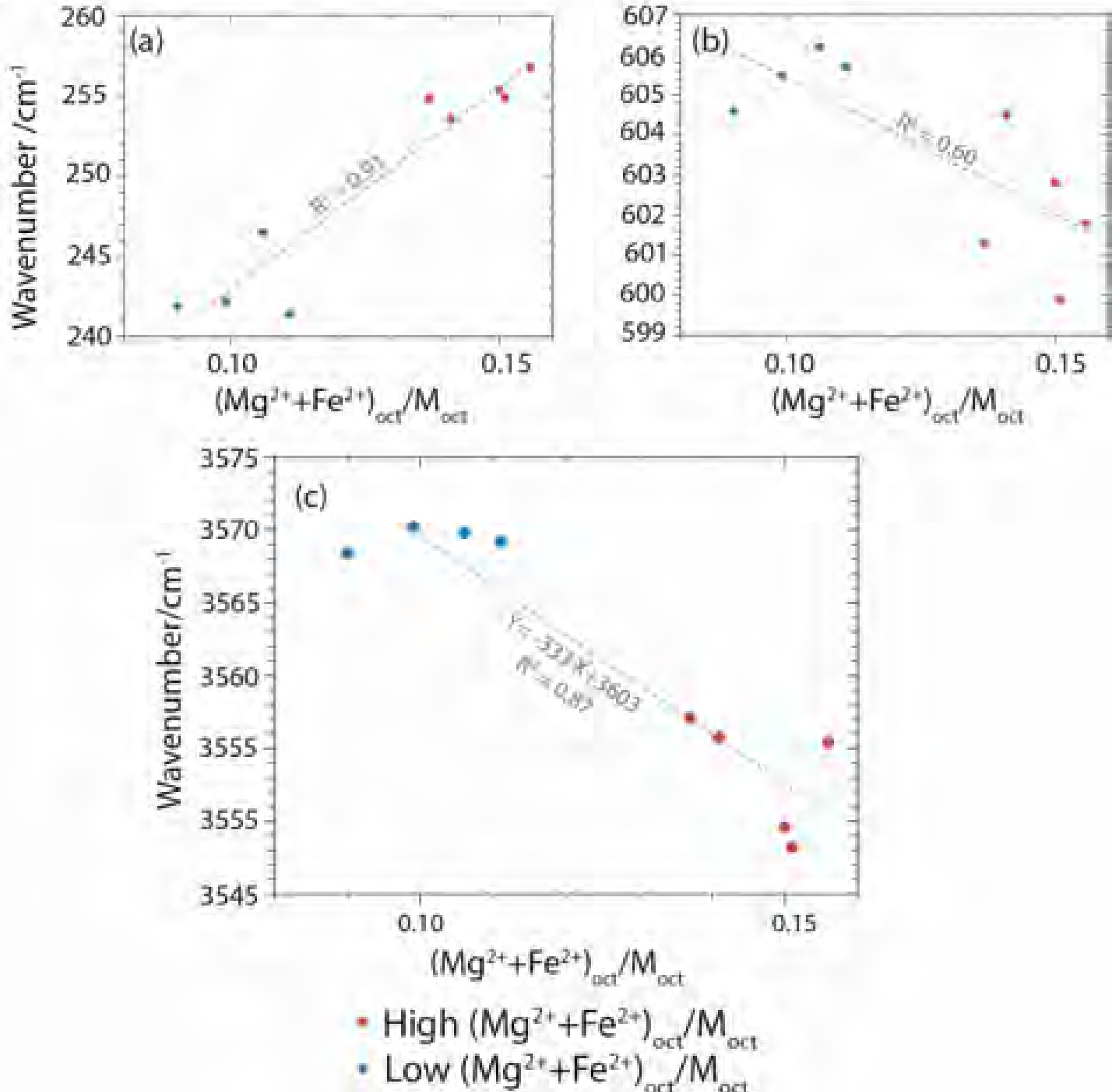
(a)
Wavenumber /cm-1
260
255
250
245
240
0.10
0.15
(Mg2++Fe2+)oct/Moct
(b)
607
606
605
604
603
602
601
600
599
0.10
0.15
(Mg2++Fe2+)oct/Moct
(c)
Wavenumber/cm-1
3575
3570
3565
3560
3555
3555
3545
0.10
0.15
(Mg2++Fe2+)oct/Moct
High (Mg2++Fe2+)oct/Moct
Low (Mg2++Fe2+)oct/Moct

Fig. 8

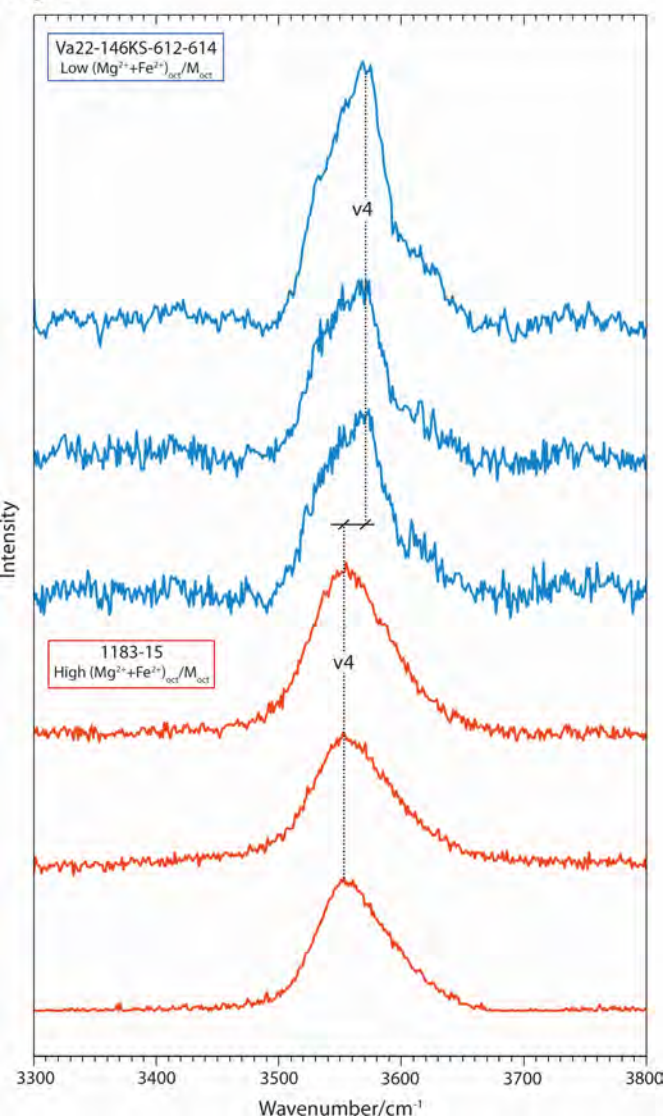
Va22-146KS-612-614
Low $(Mg^{2+}+Fe^{2+})_{oct}/M_{oct}$
v4
1183-15
High $(Mg^{2+}+Fe^{2+})_{oct}/M_{oct}$
v4
Intensity
3300
3400
3500
3600
3700
3800
Wavenumber/cm^{-1}

Fig. 9

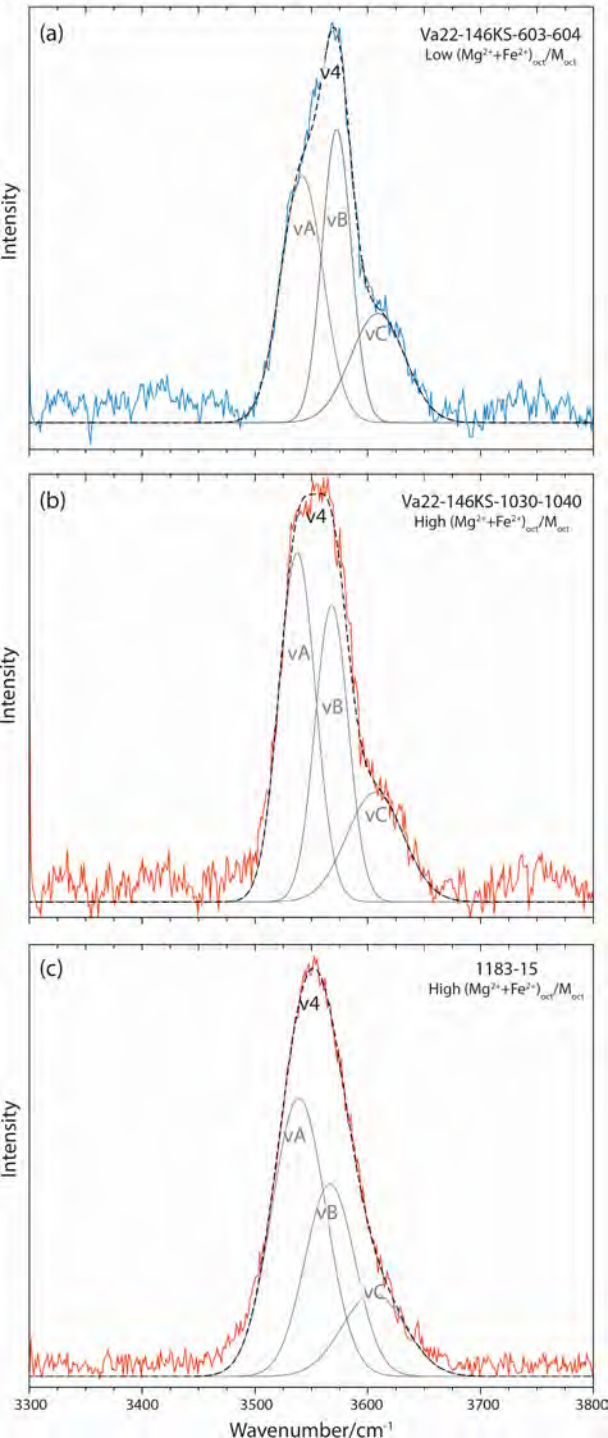
(a)
Va22-146KS-603-604
Low (Mg2++Fe2+)oct/Moct
v4
vA
vB
vC
Intensity
(b)
Va22-146KS-1030-1040
High (Mg2++Fe2+)oct/Moct
v4
vA
vB
vC
Intensity
(c)
1183-15
High (Mg2++Fe2+)oct/Moct
v4
vA
vB
vC
Intensity
3300
3400
3500
3600
3700
3800
Wavenumber/cm-1

Fig. 10

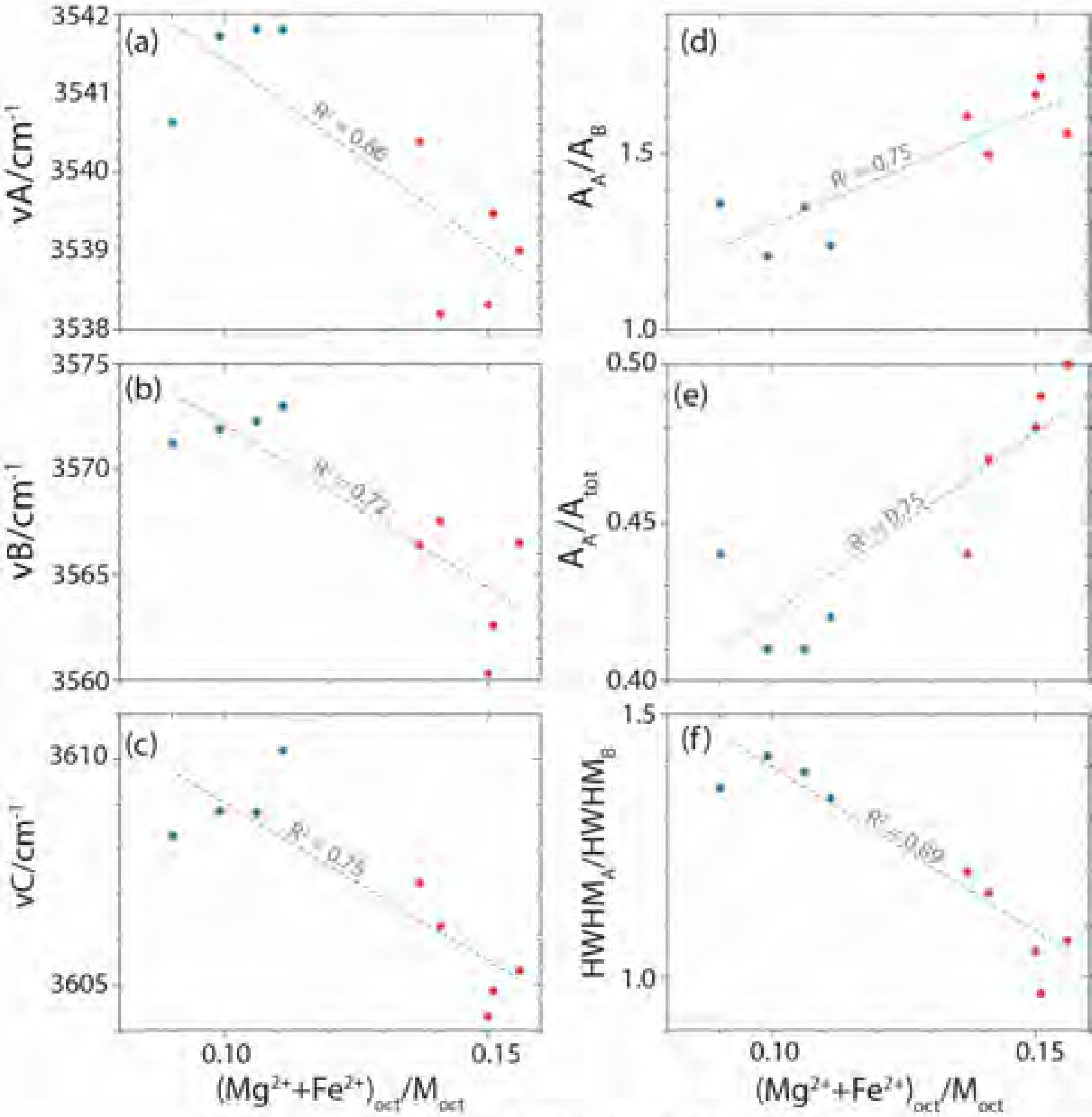
(a)
(b)
(c)
(d)
(e)
(f)
vA/cm-1
vB/cm-1
vC/cm-1
AA/AB
AA/Atot
HWHMA/HWHMB
3542
3541
3540
3539
3538
3575
3570
3565
3560
3610
3605
1.5
1.0
0.50
0.45
0.40
0.10
0.15
(Mg2++Fe2+)oct/Moct
High (Mg2++Fe2+)oct/Moct
Low (Mg2++Fe2+)oct/Moct

Fig. 11

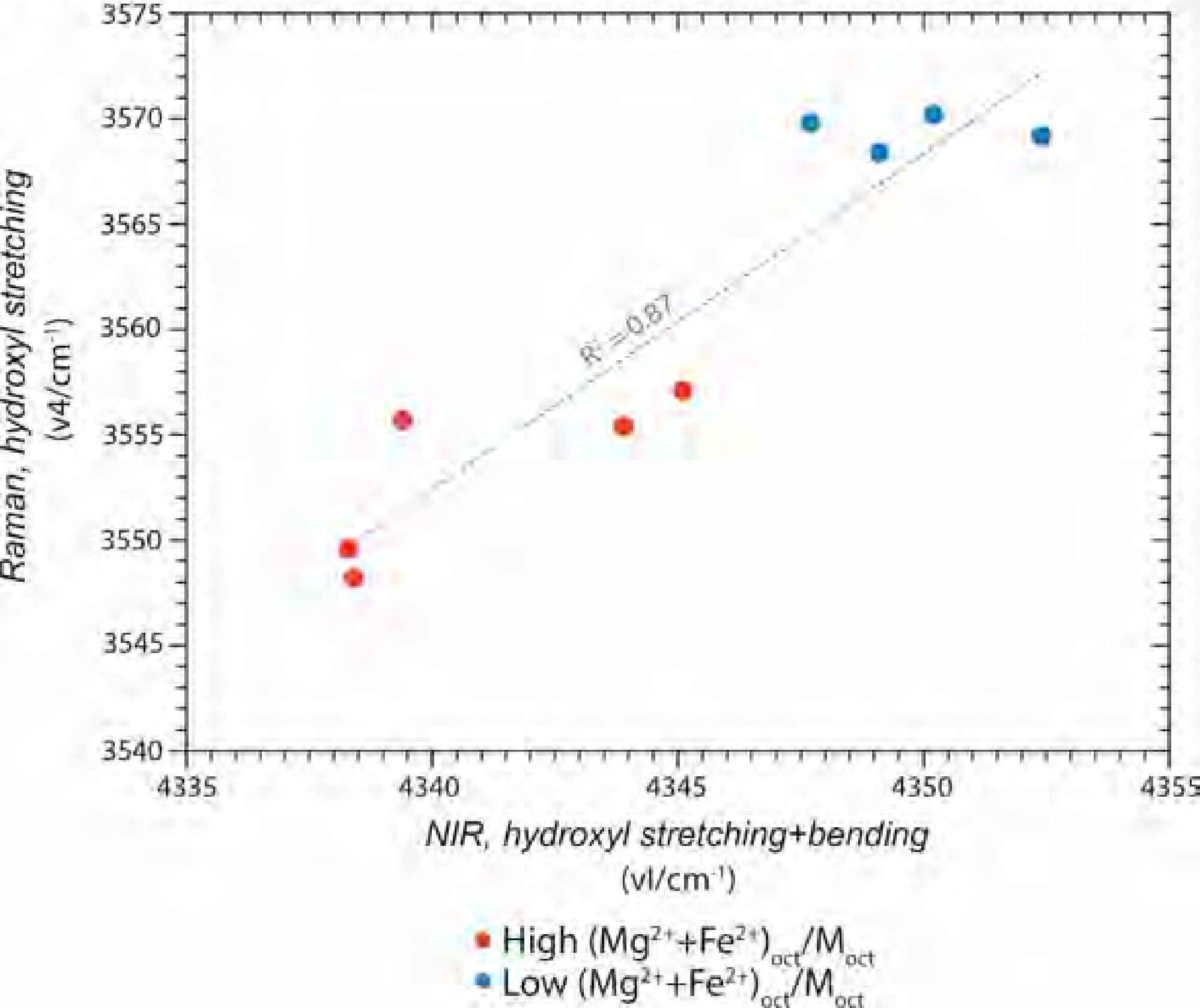
3575
3570
3565
3560
3555
3550
3545
3540
4335
4340
4345
4350
4355
Raman, hydroxyl stretching
(v4/cm-1)
R2=0.87
NIR, hydroxyl stretching+bending
(vl/cm-1)
High (Mg2++Fe2+)oct/Moct
Low (Mg2++Fe2+)oct/Moct